國立臺灣大學工學院工程科學及海洋工程學系

碩士論文

Department of Engineering Science and Ocean Engineering
College of Engineering
National Taiwan University

Master Thesis

基於船舶減阻之高速排水型單體船水翼設計優化

The Optimization of Hydrofoil Design for Resistance Reduction of a High-Speed Displacement Monohull Vessel

林禹彤

Yu-Tung Lin

指導教授：趙修武 博士

Advisor: Dr.-Ing. Shiu-Wu Chau

中華民國 112 年 7 月

July, 2023

doi:10.6342/NTU202304124

doi:10.6342/NTU202304124

Abstract

This study aims to obtain an optimized hydrofoil design for the calm-water resistance reduction of a high-speed displacement monohull vessel at $Fn = 0.6$. The target hull form is the NPL hull form with length of about 42 meters and displacement of 247.18 tons. The NACA0015 airfoil is selected for the section design of the hydrofoil installed on the hull. The design parameters of the hydrofoil are the chord length, aspect ratio, longitudinal and vertical installation positions, and installation angle. The computational fluid dynamics (CFD) software STAR-CCM+ is used to predict the calm-water ship resistance with the hydrofoil installed at the ship speed of 23.7 knots ($Fn = 0.6$). The CFD resistance prediction is adopted to train a deep neural network (DNN) model with the help of MATLAB. The proposed DNN model consists of five hidden layers with 8, 7, 6, 5, and 5 neurons, respectively, and has a mean absolute percentage error (MAPE) of 0.40%. The proposed DNN model is then used to predict the optimized design parameters of the hydrofoil. With the target resistance and the given range of design parameters, various parameter combinations are explored to identify the best design parameters that meet the target resistance. The CFD and DNN predictions of the ship resistance for the optimized hydrofoil design differ by 3.0%. After the introduction of the optimized hydrofoil design, the ship resistance is reduced by 24.9% when compared to the bare hull. Although the ship resistance is optimized for $Fn = 0.6$, the optimized hydrofoil design is able to reduce the running trim angle by 58.4% to 113.9%, the dynamic sinkage by 7.6% to 77.1%, and the ship resistance by 14.1% to 34.5% for $Fn = 0.3$ to 0.9.

Keywords: High-speed displacement monohull, Hydrofoil, Resistance reduction, Computational fluid dynamics, Running trim, Dynamic sinkage, Deep neural network

doi:10.6342/NTU202304124

doi:10.6342/NTU202304124

摘要

本研究旨在優化高速排水型單體船的水翼設計，藉此減少船舶靜水航行總阻力。本研究目標船形為 NPL 開放船形，船長約 42 公尺，排水量為 247.18 噸；安裝於船體的水翼則使用 NACA0015 翼形。本研究選定弦長、展弦比，縱向與垂向安裝位置以及安裝角度為水翼設計參數，使用計算流體力學軟體 STAR-CCM+預測船速 23.7 節（$Fn = 0.6$）具水翼的靜水阻力和姿態，利用 MATLAB 軟體以阻力預測結果訓練深度神經網路模型。本研究使用的深度神經網路模型具五層隱藏層，各層分別有 8、7、6、5 和 5 個神經元，平均絕對百分比誤差值為 0.40%。本研究接著使用深度神經網路模型預測水翼的優化設計參數，透過考慮目標阻力和設計參數範圍，深度神經網路模型會進行各參數的排列組合，找出符合目標阻力的最佳設計參數。計算流體力學和深度神經網路預測具優化水翼設計的船舶靜水航行總阻力相差 3.0%。具優化設計水翼船舶的阻力較裸船減少 24.9%。本研究雖然針對 $Fn = 0.6$進行阻力優化，在$Fn = 0.3$到 0.9，安裝優化水翼的 NPL 船形預測減少 58.4%到 113.9%的俯仰角變化，7.6%到 77.1%的動態下沉量以及 14.1%到 34.5%的阻力值。

關鍵詞：高速排水型單體船，水翼，阻力優化，計算流體力學，航行俯仰角，動態下沉量，深度神經網路

doi:10.6342/NTU202304124

doi:10.6342/NTU202304124

Contents

doi:10.6342/NTU202304124

doi:10.6342/NTU202304124

Nomenclature

Latin symbols

A_M	Midship area of ship	[m^2]
A_{WET}	Wetted surface area of ship	[m^2]
Ⓐ	Wetted surface coefficient	[-]
a	Installation angle of hydrofoils	[°]
a_i	Volume fraction of the ith fluid in a cell unit	[-]
a_1	Equation constant	[-]
a^*	Equation constant	[-]
B_{OA}	Breadth overall of ship	[m]
B_{WL}	Breadth on designed waterline of ship	[m]
b_j^h	Bias of hidden layer for the jth neuron in DNN model	[-]
b_k^o	Bias of output layer for the kth output in DNN model	[-]
c	Chord length	[m]
C^{DOWN}	Downstream swept distance estimation factor	[-]
C^{UP}	Upstream swept distance estimation factor	[-]
C_a	Sharpening factor	[-]
C_B	Block coefficient	[-]
C_D	Drag coefficient	[-]
C_F	Flat-plate resistance coefficient	[-]
C_L	Lift coefficient	[-]
C_M	Midship coefficient	[-]
$c_{p,dym}$	Dynamic pressure coefficient	[-]
C_R	Residuary resistance coefficient	[-]
C_T	Total resistance coefficient	[-]
c_T	Equation constant	[-]
ΔC_F	Roughness allowance	[-]

doi:10.6342/NTU202304124

D	Depth of ship	[m]
d	Draught of ship	[m]
d_1	The shortest distance from wall	[m]
dx	Characteristic cell size	[-]
dx_n	Characteristic cell size of the nth grid level	[-]
E_{R_T}	Discretization error	[-]
e	Loss function of DNN model	[-]
F_D	Drag force	[kN]
F_L	Lift force	[kN]
Fn	Froude number	[-]
Fn_∇	Froude number based on displacement volume	[-]
g	Gravitational acceleration	[m/s^2]
g_i	Gravitational acceleration in i direction	[m/s^2]
I_{final}	Final indicators of AMR criterion	[-]
I_0	Initial indicators of AMR criterion	[-]
K	Number of parts for data splitting	[-]
k	Turbulent kinetic energy	[N·m]
LCB	Longitudinal center of buoyancy	[m]
L_{OA}	Length overall of ship	[m]
L_{WL}	Length on designed waterline of ship	[m]
l_i	Input of DNN model	[-]
m_j^h	Transferred value of hidden layer in DNN model of the jth neuron	[-]
Ⓜ	Length-displacement ratio	[-]
N_{AMR}	Update frequency of AMR solver	[-]
N	Number of grids	[-]
N_n	Number of grids of the nth grid level	[-]
n	Normal vector	[-]
n_i	Normal vector of planes on boundaries	[-]

doi:10.6342/NTU202304124

$P_n(n)$	Purelin function	[-]
p	Pressure of the flow field	[Pa]
p_{dym}	Dynamic pressure of the flow field	[Pa]
p_s	Hydrostatic pressure of flow field	[Pa]
Re	Reynolds number	[-]
R_F	Flat-plate resistance of ship	[kN]
R_P	Pressure resistance of ship	[kN]
R_R	Residuary resistance of ship	[kN]
R_S	Shear resistance of ship	[kN]
R_T	Ship resistance	[kN]
R_T^{CFD}	Ship resistance predicted by CFD	[kN]
R_T^{DNN}	Ship resistance predicted by DNN	[kN]
R_T^{∞}	Grid-independent ship resistance	[kN]
R_T^n	Ship resistance of the nth grid level	[kN]
r_i	Resolution criterion for interface detection	[-]
S	Shear rate	[1/s]
S_{ij}	Shear rate tensor	[1/s]
s	Span	[m]
T^{DOWN}	Time of the next AMR event (downstream)	[s]
T^{UP}	Time of the next AMR event (upstream)	[s]
T_s	Time scale	[-]
$T_g(n)$	Tansig function	[-]
t	Current time step	[s]
Δt	Time step size	[s]
u_i	Flow velocity in i direction	[m/s]
V	Total volume of a cell	[m^3]
V_A	Volume of the air in a cell	[m^3]
V_W	Volume of the water in a cell	[m^3]
$\mathbf{v}$	Velocity vector	[m/s]

doi:10.6342/NTU202304124

$\mathbf{v}_{c,i}$	Sharpening velocity vector of the ith fluid in a cell	[m/s]
$\mathbf{v}_{d,i}$	Diffusion velocity vector of the ith fluid in a cell	[m/s]
v_m	Model speed	[m/s]
v_s	Ship speed	[m/s]
w_{ij}^h	Weight of hidden layer for the ith input and the jth neuron in DNN model	[-]
w_{jk}^o	Weight of output layer for the jth neuron and the kth output in DNN model	[-]
x_i	Cartesian coordinate in i direction	[m]
y_k	The kth exact value of database for DNN model training	[-]
$\hat{y}_k$	The kth output of DNN model	[-]

doi:10.6342/NTU202304124

Greek symbols

α	Angle of attack	[°]
β	Equation constant	[-]
β^*	Equation constant	[-]
γ	Equation constant	[-]
Δ	Displacement of ship	[tons]
δ	Dynamic sinkage	[m]
δ_{ij}	Kronecker delta	[-]
η	Non-dimensional free surface elevation	[-]
θ	Running trim	[°]
κ	von Kármán constant	[-]
Λ	Aspect ratio of hydrofoil	[-]
λ	Scale ratio	[-]
μ	Dynamic viscosity	[Pa·s]
μ_t	Turbulent viscosity	[Pa·s]
μ_{SW}	Dynamic viscosity of seawater	[Pa·s]
μ_W	Dynamic viscosity of water	[Pa·s]
ω	Specific turbulence dissipation rate	$[1/s]$
ρ	Density of the ith fluid in a cell unit	[kg/ m^3]
ρ_{SW}	Density of seawater	[kg/ m^3]
ρ_W	Density of water	[kg/ m^3]
σ_k	Equation constant	[-]
σ_ω	Equation constant	[-]
ϕ^∞	Grid-independent value of ϕ	[-]
ϕ^n	Generic field variable of the nth grid level	[-]
∇	Displacement volume of ship	[m^3]

doi:10.6342/NTU202304124

doi:10.6342/NTU202304124

List of Figures

doi:10.6342/NTU202304124

doi:10.6342/NTU202304124

List of Tables

doi:10.6342/NTU202304124

doi:10.6342/NTU202304124

Chapter 1 Introduction

1.1 Literature Review

1.1.1 Applications of Hydrofoils on Ships

The usage of hydrofoils on ships has a long history, where they are employed for reducing roll motions or changing the running trim angle by the lift force. Previous studies [1-5] have examined the impact of hydrofoils on reducing running trim angles. Studies [1, 2] investigated the hydrofoils installed near the bow of container ships, while the study [3] examined them installed at the midship of a cruise ship. These studies found that even small installation angles of hydrofoils can improve the ship's attitude. However, the additional drag and draught change caused by the hydrofoils possibly led to poor resistance performance.

Conversely, studies [4, 5] found that hydrofoils installed near the stern helped to reduce the running trim angle and dynamic sinkage as well as ship resistance. Study [5] developed a systematic method for individually investigating the effect of installation location, angle of attack, and foil geometry without considering the combined effect of these parameters. Because these studies did not consider the combined effect of the design parameters of hydrofoils on ship motion, they failed to provide a comprehensive approach to obtain an optimized design. Therefore, there is a need for further research on developing a comprehensive strategy to acquire optimized design parameters of hydrofoils for achieving the target resistance performance of ships.

doi:10.6342/NTU202304124

1.1.2 Deep Learning

Based on statistical data, regression analysis has traditionally been used to find the dependence of ship resistance on hull form [6]. A successful regression method requires a proper selection of parameters. Therefore, if the parameters are not well selected, it is difficult to obtain good results through regression analysis. Deep learning can fill this gap by providing predicted answers based on extensive databases.

Deep learning models are commonly constructed by Neural networks (NNs). They are similar to biological neural networks in a human brain, and model patterns of human learning. Recurrent neural networks (RNNs) [7] are good for training sequential data like music and sentences, while convolutional neural networks (CNNs) [8] are ideal for grid-patterned data such as images. The deep neural network (DNN) [9] model, which trains data only in a forward direction from input to output, is selected for this study because it fits the need of this problem.

Deep learning models have been applied to various ship topics with great success. In the context of ship resistance optimization, the studies [10] and [11] employed the free-form deformation, the study [12] used the principal component analysis (PCA) to construct different hull forms, and deep neural networks were trained to predict ship resistance for each hull form to optimize resistance. The study [13] utilized the pressure distribution, free-surface elevation, and wake images of different ship forms as inputs to train a CNN model for predicting their hydrodynamic performance and resistance. Successful cases also exist in the areas of sea state and ship motion prediction. The research [14] and [15] respectively employed neural networks trained with sea state parameters and wave characteristics to forecast short-term sea states and waves. The research [16] trained a neural network with hull form parameters to predict the ship's seakeeping performance, while the studies [17] and [18] trained neural networks to

doi:10.6342/NTU202304124

predict short-term ship motions. The investigations [19] and [20] applied neural networks to ship structure applications, where the ultimate strength and fatigue failure were predicted using transverse structural information. The investigations [21] and [22] trained neural networks using hull form data, ocean environmental data, and ship speed to predict the required engine power. The study [23] predicted the fuel consumption using the engine and propulsion system information, flow field data, and dead weight. The study [24] utilized the public data such as ship and engine data, weather data, etc., to predict the energy efficiency operational indicators (EEOI).

The above literature presents various research approaches utilizing deep learning models, serving as valuable references for this study. This research aims to apply neural networks to identify hydrofoil designs that can reduce ship resistance and an effective design strategy to achieve this goal.

doi:10.6342/NTU202304124

1.2 Motivation and Framework

Fast-displacement vessels, due to their ability to support a displacement hull with the speed of a planing hull [25-27], are widely used in various applications, such as yachts, patrol vessels, and warships. However, they commonly need appendages to reduce the significant running trim at high speeds, such as trim wedge or interceptor [28, 29].

The trim wedge and interceptor are compact appendages that effectively reduce the running trim angle during navigation. However, at low Froude numbers, interceptors may induce larger running trim angles, resulting in a drag increase. The trim wedge generally exhibits good performance at low Froude numbers but it provides a comparatively smaller reduction compared to the interceptor in the running trim angle. Alternatively, hydrofoils are a kind of appendage that also serves the purpose of reducing the running trim angle. Its notable advantage lies in its adaptability to various hull forms through the adjustment of various design parameters. The hydrofoils are generally installed with a control system to offer an ability to dynamically regulate the ship's attitude in real-time, accommodating varying sea conditions and offering great flexibility.

Due to the complexity of hydrofoil design, assistance tools are required for the design process. Deep learning models can assist in generalizing the correlation between the design parameter combinations and the corresponding resistance as well as identifying the most favorable parameter combination. Among deep learning models, DNNs are suitable for this study because they have multiple hidden layers, enabling them to effectively handle non-linear correlations. Moreover, their generalization performance improves with large datasets, making them well-suited for this research.

This study aims to improve the resistance performance of a high-speed displacement monohull vessel by optimizing its hydrofoil design. First, computational fluid dynamics

doi:10.6342/NTU202304124

(CFD) approach is employed to generate a database of the ship resistance alongside attitude for various hydrofoils designs. The database is then used to train a DNN model in searching for optimized design parameters for resistance reduction. The proposed DNN model is subsequently validated using several test cases. Finally, the optimized hydrofoil design identified by the DNN model is assessed through the CFD model to evaluate its impact on resistance performance. The proposed framework is given in Figure 1.

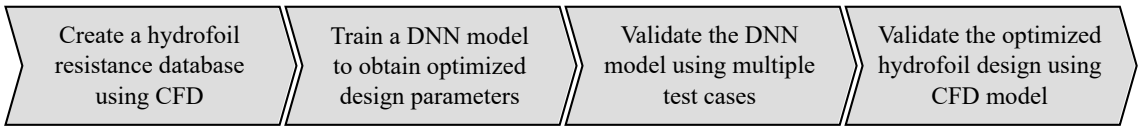

Figure 1: Framework of the research process

doi:10.6342/NTU202304124

doi:10.6342/NTU202304124

Chapter 2 Geometry of Ship and Hydrofoil

2.1 Dimensionless Parameters

The hydrodynamics characteristics of a ship and the flow field are usually described by the Froude number (Fn) and the displacement Froude number (Fn_∇), which are dimensionless parameters representing the ratio of inertia forces to gravitational forces. Eq. (2.1.1) defines the Froude number, while Eq. (2.1.2) defines the displacement Froude number as follows:

$$Fn = \frac{v_s}{\sqrt{gL_{WL}}}, \tag{2.1.1}$$

$$Fn_\nabla = \frac{v_s}{\sqrt{g\nabla^{1/3}}}, \tag{2.1.2}$$

where v_s is the ship speed, g represents the gravitational acceleration, L_{WL} is the length of designed waterline, and ∇ is the displacement volume. Another dimensionless parameter that describes the flow field, the Reynolds number (Re), represents the ratio of inertia forces to viscous forces, and is defined as follows:

$$Re = \frac{\rho_W v_s L_{WL}}{\mu_W}, \tag{2.1.3}$$

where ρ_W is the water density, and μ_W is the water dynamic viscosity. In this study, ρ_W is 1023.9808 kg/m^3, and μ_W is 0.001077 Pa·s.

doi:10.6342/NTU202304124

2.2 Hull Form

The coordinate system utilized in this study is depicted in Figure 2. The x-axis originates from the ship's transom towards the bow, where L_{OA} the length overall. The y-axis points towards the port side, while the z-axis follows the upward direction of the ship. B_{WL} and B_{OA} denote the breadth of the designed waterline and overall breadth, respectively. D denotes the ship depth, and d is the draught. The block and midship coefficients (C_B and C_M) of the ship are respectively defined as follows:

$$C_B = \frac{\nabla}{L_{WL}B_{WL}d}, \tag{2.2.1}$$

$$C_M = \frac{A_M}{B_{WL}d}, \tag{2.2.2}$$

where A_M represents the midship section area of the ship. The length-displacement ratio Ⓜ and wetted surface coefficient Ⓐ are two dimensionless parameters that represent the ship's properties and are defined as follows:

$$Ⓜ = \frac{L_{WL}}{\nabla^{1/3}}, \tag{2.2.3}$$

$$Ⓐ = \frac{A_{WET}}{\nabla^{2/3}}, \tag{2.2.4}$$

where A_{WET} is the wetted surface of the ship model. The ship displacement is defined as the displacement volume (∇) times the water density (ρ_W), as Eq. (2.2.5) shows.

$$\Delta = \rho_W \nabla. \tag{2.2.5}$$

The hull form utilized in this study is selected from a systematic series of high-speed round-bilged displacement monohulls proposed by the Nation Physical Laboratory (NPL) [30]. Specifically, the employed model is 100A, which is the basic hull form within the series (i.e., the parent hull form). The ship data is listed in Table 1, and its line drawing is depicted in Figure 3. Although the design data and experiments are based on the model

doi:10.6342/NTU202304124

scale, this study focuses on designing hydrofoils for full-scale vessels, where the scale ratio (λ) is 16.21, because they are more aligned with practical engineering applications.

This ship series is designed to operate in the range of $Fn = 0.30$~1.19. Since this study focuses on the high-speed region, $Fn = 0.6$ is chosen as the design speed, where the corresponding target speed is 23.7 knots or 12.18 m/s.

doi:10.6342/NTU202304124

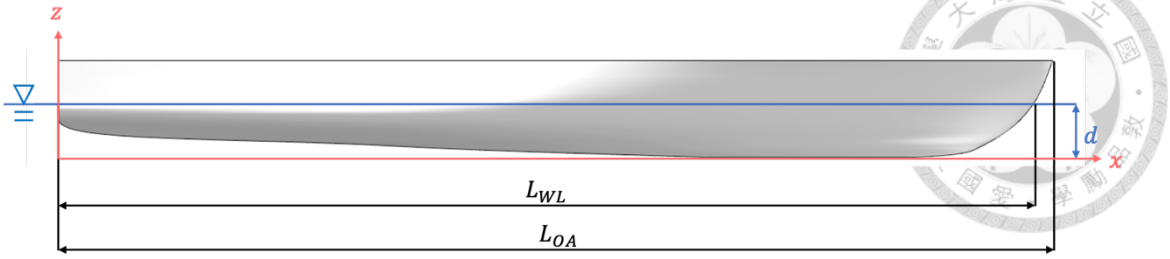

(a) $x-z$ plane

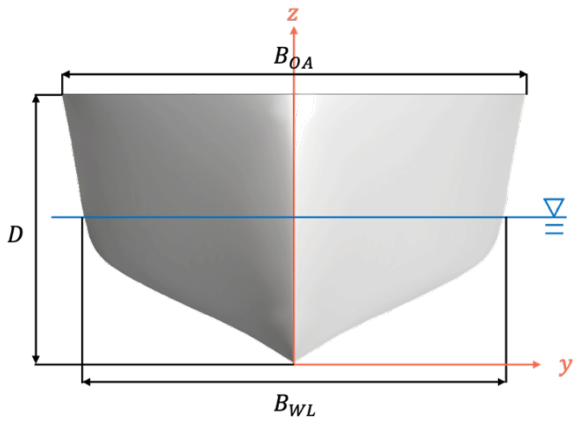

(b) $y-z$ plane

Figure 2: Principal dimensions of ship

Table 1: Data of full-scale NPL hull 100A

L_{OA} [m]	L_{WL} [m]	B_{OA} [m]	B_{WL} [m]	D [m]	d [m]	LCB [m]
42.004	41.181	7.119	6.448	4.116	2.267	17.897
∇ [m^3]	Δ [tons]	λ [-]	A_M [m^2]	A_{WET} [m^2]	C_B [-]	C_M [-]
241.19	247.18	16.21	7.60	274.97	0.40	0.52
Ⓜ [-]	Ⓐ [-]	Fn [-]	Fn_∇ [-]	Re [-]	v_s [m/s]	v_s [kt]
6.585	7.17	0.6	1.56	4.87×10^8	12.18	23.7

doi:10.6342/NTU202304124

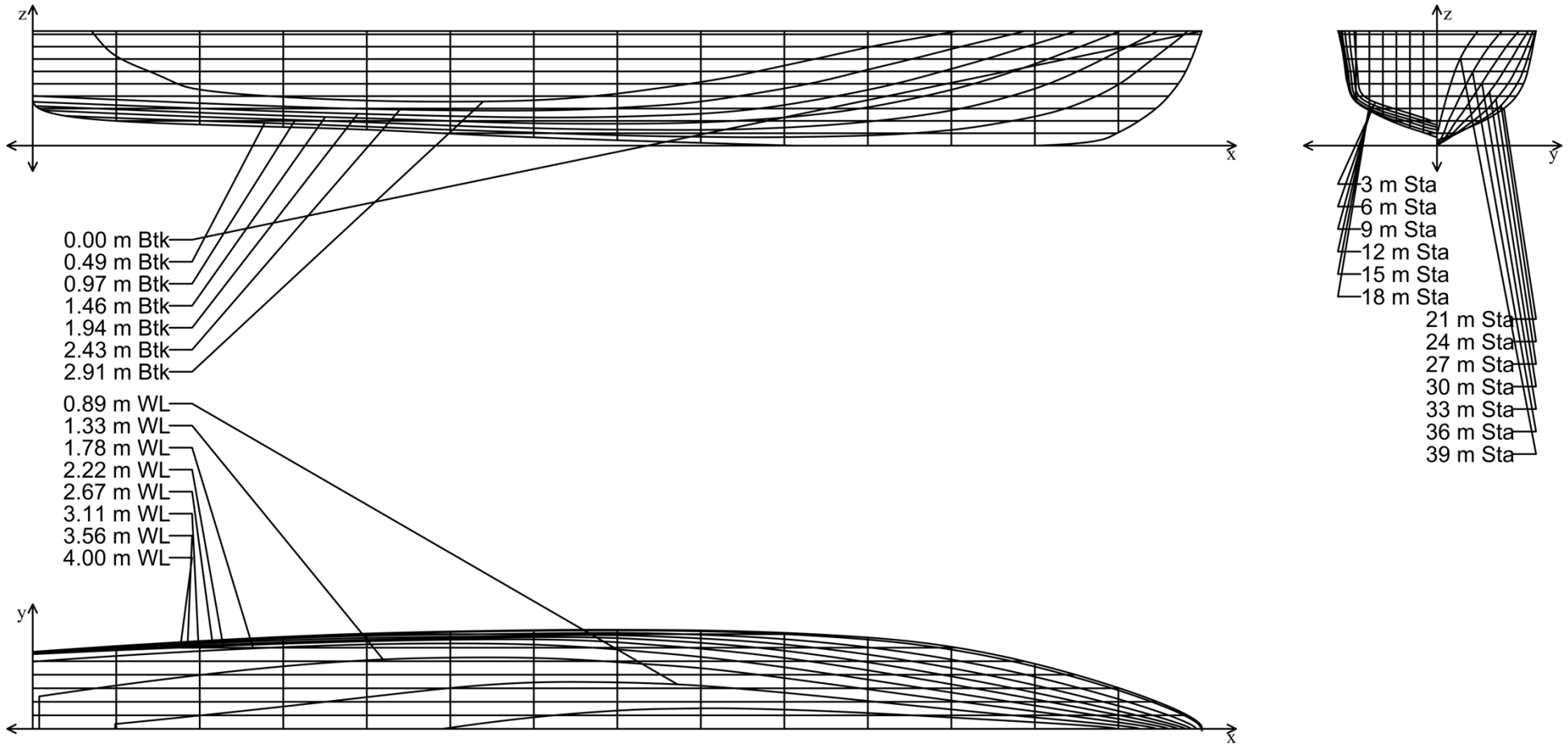

Figure 3: Lines drawing of NPL hull form 100A

doi:10.6342/NTU202304124

2.3 Hydrofoil

Figure 4 defines the adopted non-tapered hydrofoil, where s denotes the span, and c is the chord length. The aspect ratio (Λ) is defined by s and c as follows:

$$\Lambda = s/c. \tag{2.3.1}$$

This study uses NACA0015 for the foil section of hydrofoils. The first two digits of the serial number NACA0015 indicate that this foil section has no camber, and is symmetrical. The last two numbers mean that it has a thickness-to-chord ratio of 15% at its maximum thickness.

Figure 5 shows the forces acting on a foil section, where F_D is the drag force, F_L is the lift force, and α is the angle of attack (AOA). To investigate the lift and drag performance of a NACA0015 airfoil, a CFD approach is employed, where the lift and drag coefficients are calculated at various angles of attack. The non-dimensional drag and lift coefficients, C_D and C_L, are defined as follows [31]:

$$C_D = \frac{F_D}{(0.5\rho_W c {v_s}^2)}, \tag{2.3.2}$$

$$C_L = \frac{F_L}{(0.5\rho_W c {v_s}^2)}. \tag{2.3.3}$$

The relationship between the AOA and the drag and lift coefficients is illustrated in Figure 6. As the absolute value of the AOA increases, the drag and lift coefficients also increase. The direction of the lift force is consistent with the sign of the AOA, while the direction of the drag force is always the same. When the AOA is small, the lift coefficient closely match the analytical solution from the thin airfoil theory [32], given by Eq. (2.4.4):

$$C_L = 2\pi\alpha, \tag{2.3.4}$$

where the lift coefficient is linearly proportional to the AOA.

doi:10.6342/NTU202304124

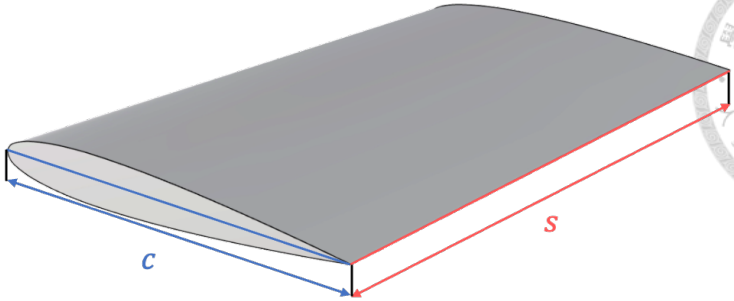

Figure 4: Principal dimensions of a non-tapered hydrofoil

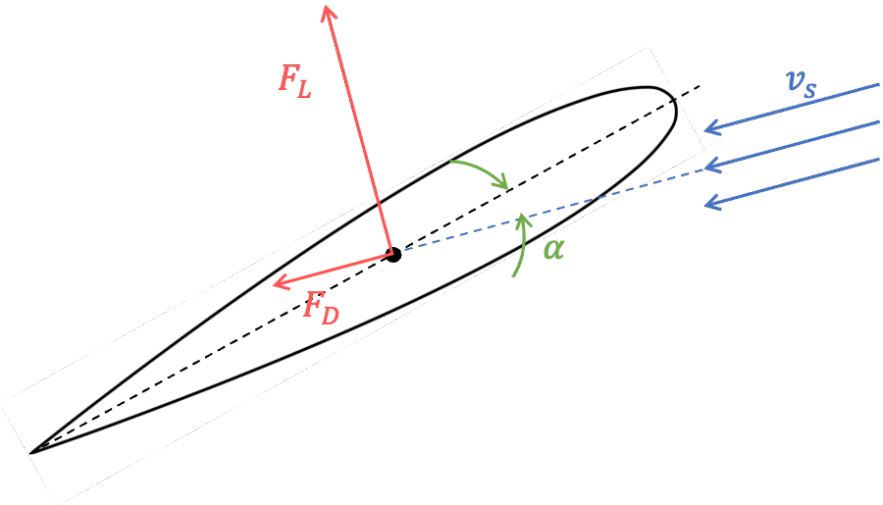

Figure 5: Forces acting on a foil section

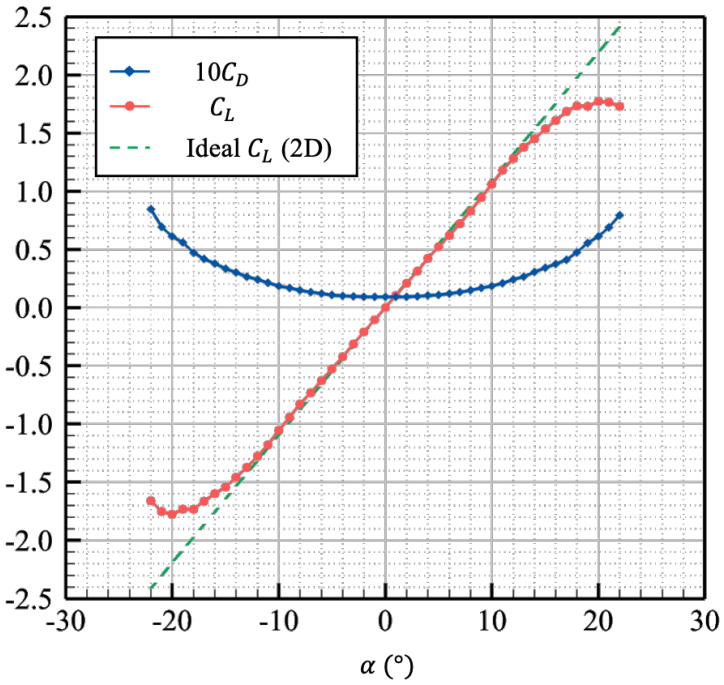

Figure 6: Lift and drag coefficients of NACA0015

doi:10.6342/NTU202304124

2.4 Design Parameters

Table 2 presents the ranges and values of design parameters for the installed hydrofoil used in creating the resistance database. For delivering a sufficient pitching moment, the positions between $x = 9$ m and $x = 31$ m are excluded. Because the hydrofoil has to be installed at a suitable depth below the free surface to ensure its proper performance, its vertical location is limited between $z = 0.2$ m to $z = 1.4$ m. Figure 7 illustrates possible selected installation positions of the hydrofoil. The installation angles (ψ) of the hydrofoils are an additional design parameter that influences the angle of attack. At the target ship speed, the ship tends to trim by stern, so the angle of attack must be positive for a stern hydrofoil to produce a pitching moment that reduces the running trim angle, where positive installation angles are required. Conversely, the angle of attack becomes negative for a bow hydrofoil, so negative installation angles are required. The direction of lift force dependent on the installation angle is illustrated in Figure 8.

Apart from the installation positions and angles, the dimensions of the hydrofoil can also affect its lift and drag performance. Therefore, this study investigates four chord lengths and four aspect ratios to examine their impact on the resistance and attitude of the ship. Figure 9 displays the NPL hull with hydrofoils installed at various locations. For simplicity, the outermost edge of each hydrofoil is always at the same y-coordinate. Hence some of them are farther away from the ship, while others are closer to the ship. Therefore, when constructing a model with a hydrofoil, this study uses a cylindrical support to connect the hydrofoil to the ship.

Due to the curvature of the hull surface, certain installation positions and angles are not feasible. Consequently, these infeasible parameter combinations are excluded from this study. As a result, a total of 1541 possible parameter combinations are obtained,

doi:10.6342/NTU202304124

where each features a combination of distinct installation positions, angles, and dimensions.

Table 2: Ranges of design parameters

	x [m]		z [m]	ψ [°]	c [m]	Λ [-]
Ranges	1 – 9,	31 – 39	0.2 – 1.4	0 – 14	1.05 – 1.81	1.0 – 1.6
Values	1, 5, 9	31, 35, 39	0.2, 0.6, 1.0, 1.4	0, 2, 4, 6, 8, 10, 12, 14	1.05, 1.26, 1.51, 1.81	1.0, 1.2, 1.4, 1.6

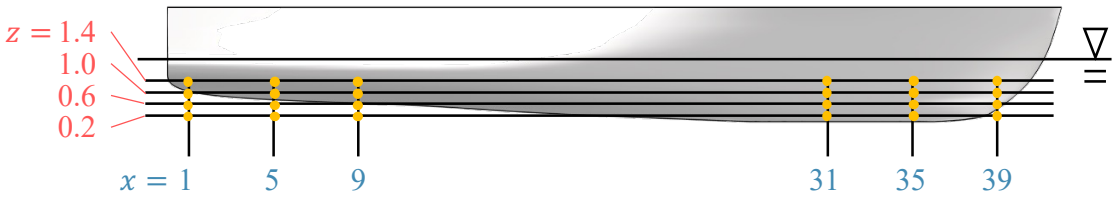

Figure 7: Possible installation positions of hydrofoils

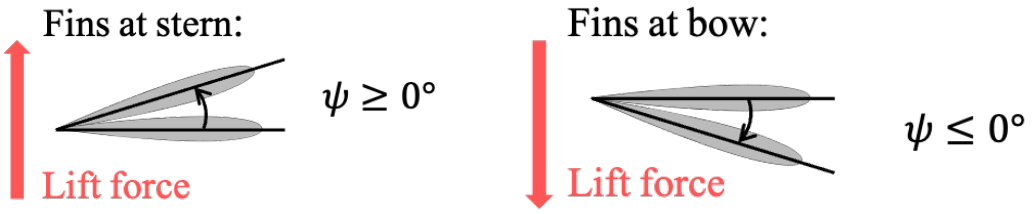

Figure 8: Installation angle used for the hydrofoil at bow or stern

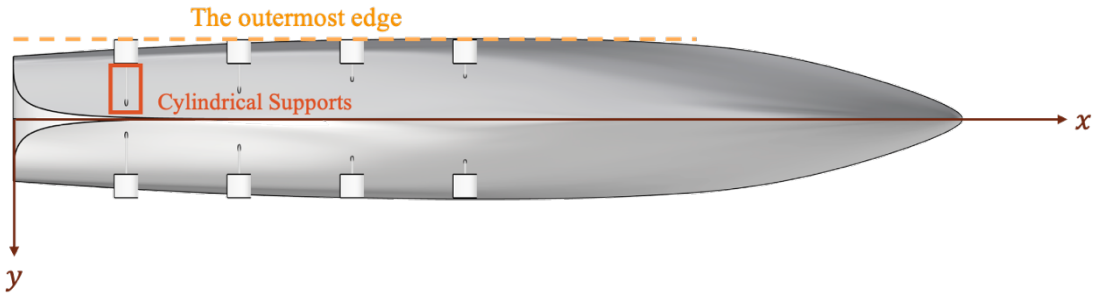

Figure 9: NPL hull with hydrofoil

doi:10.6342/NTU202304124

doi:10.6342/NTU202304124

Chapter 3 CFD Model

This study utilizes the CFD software STAR-CCM+ [33] to predict the calm-water resistance of a ship. STAR-CCM+ employs the finite volume method to discretize the governing equations of the flow field, and utilizes the volume of fluid method to model the free surface. The software then solves the governing equations through an iterative process.

3.1 Governing Equations

This study assumes that the flow is incompressible and turbulent. The continuity equation, Eq. (3.1.1), and momentum equations, Eq. (3.1.2) are used as governing equations, which are expressed as follows:

(a) Continuity equation

$$\frac{\partial(\rho u_i)}{\partial x_i} = 0, \tag{3.1.1}$$

(b) Momentum equations

$$\frac{\partial(\rho u_i)}{\partial t} + \frac{\partial(\rho u_i u_j)}{\partial x_j} = -\frac{\partial p}{\partial x_i} + \frac{\partial}{\partial x_j}\left\{\mu\left(\frac{\partial u_j}{\partial x_i} + \frac{\partial u_i}{\partial x_j}\right)\right\} + \frac{\partial}{\partial x_j}\left(-\rho\overline{u_i' u_j'}\right) + g_i, \tag{3.1.2}$$

where ρ denotes the density of fluids, p is the total pressure of the flow field, μ is the dynamic viscosity of fluid, $\rho\overline{u_i' u_j'}$ is Reynolds stress, and x_i, u_i, and g_i represent the Cartesian coordinate, flow velocity, and gravitational force in the i direction, respectively.

doi:10.6342/NTU202304124

3.2 Turbulence Model

The turbulence model used in this study is the SST $k-\omega$ model, which is described by Eq. (3.2.1) and Eq. (3.2.2) that govern the transport behavior of the turbulent kinetic energy (k) and its specific turbulent dissipation rate (ω).

$$\frac{\partial k}{\partial t}+\frac{\partial\left(ku_j\right)}{\partial x_j}=\frac{P}{\rho}-\beta^*\omega k+\frac{\partial}{\partial x_j}\left[\frac{1}{\rho}(\mu+\sigma_k\mu_t)\frac{\partial k}{\partial x_j}\right], \tag{3.2.1}$$

$$\begin{aligned}&\frac{\partial\omega}{\partial t}+\frac{\partial\left(\omega u_j\right)}{\partial x_j}\\&=\gamma\frac{P}{\mu_t}-\beta\omega^2+\frac{\partial}{\partial x_j}\left[\frac{1}{\rho}(\mu+\sigma_\omega\mu_t)\frac{\partial\omega}{\partial x_j}\right]+2(1-F_1)\frac{\sigma_{\omega2}}{\omega}\frac{\partial k}{\partial x_j}\frac{\partial\omega}{\partial x_j},\end{aligned} \tag{3.2.2}$$

$$P=\min\left(\tau_{ij}\frac{\partial u_i}{\partial x_i},20\beta^*\rho\omega k\right) \tag{3.2.3}$$

$$F_1=\tanh\left(\left(\min\left(\max\left(\frac{\sqrt{k}}{\beta^*\omega d_1},\frac{500}{(d_1)^2\omega}\right),\frac{4\rho\sigma_{\omega2}k}{\mathrm{CD}_{k\omega}(d_1)^2}\right)\right)^4\right), \tag{3.2.4}$$

$$\mathrm{CD}_{k\omega}=\max\left(2\rho\sigma_{\omega2}\frac{1}{\omega}\frac{\partial k}{\partial x_j}\frac{\partial\omega}{\partial x_j},\ 10^{-20}\right), \tag{3.2.5}$$

where d_1 is the shortest distance to the wall, $\beta^*=0.09$, and $\frac{\sqrt{k}}{\beta^*\omega d_1}$ represents the turbulence length scale. The Reynolds stress is defined by Eq. (3.2.6) as follows:

$$-\rho\overline{u_i'u_j'}=\mu_t\left(\frac{\partial u_j}{\partial x_i}+\frac{\partial u_i}{\partial x_j}\right)-\frac{2}{3}\rho k\delta_{ij}, \tag{3.2.6}$$

$$\mu_t=\rho kT_s, \tag{3.2.7}$$

where μ_t represents the turbulent viscosity, T_S is the time scale that is determined using Durbin's realizability constraint given by Eq. (3.2.8):

$$T_S=\min\left[\frac{1}{\left(\max\left(\frac{\omega}{a^*},\ \frac{SF_2}{a_1}\right)\right)},\frac{c_T}{\sqrt{3}S}\right], \tag{3.2.8}$$

doi:10.6342/NTU202304124

$$F_2 = \tanh\left(\left(\max\left(\frac{2\sqrt{k}}{\beta^*\omega d_1}, \frac{500\upsilon}{(d_1)^2\omega}\right)\right)^2\right), \tag{3.2.9}$$

where $a_1 = 0.31$, $a^* = 1.00$, and $c_T = 0.60$. The shear rate S is determined by the flow velocity as follows:

$$S^2 = 2S_{ij}S_{ij}, \tag{3.2.10}$$

$$S_{ij} = \frac{1}{2}\left(\frac{\partial u_i}{\partial x_j} + \frac{\partial u_j}{\partial x_i}\right). \tag{3.2.11}$$

The equation constants of the turbulent model, i.e., β, σ_k, σ_ω, and γ, given by Eq. (3.2.12) - (3.2.15), are defined by the parameters F_1, κ, and β^* as follows:

$$\beta = 0.0750F_1 + 0.0828(1 - F_1), \tag{3.2.12}$$

$$\sigma_K = 0.85F_1 + 1.00(1 - F_1), \tag{3.2.13}$$

$$\sigma_\omega = 0.500F_1 + 0.856(1 - F_1) \tag{3.2.14}$$

$$\gamma = F_1\gamma_1 + (1 - F_1)\gamma_2, \tag{3.2.15}$$

$$\gamma_1 = \frac{\beta_1}{\beta^*} - \sigma_{\omega 1}\frac{\kappa^2}{\sqrt{\beta^*}}, \tag{3.2.16}$$

$$\gamma_2 = \frac{\beta_2}{\beta^*} - \sigma_{\omega 2}\frac{\kappa^2}{\sqrt{\beta^*}}. \tag{3.2.17}$$

where $\kappa = 0.41$ is the von Kármán constant.

doi:10.6342/NTU202304124

3.3 Volume of Fluids Method

This study considers the free surface effect to predict the total resistance of a ship, where the interface between air and water is to be captured. Therefore, the volume of fluid method is used to model the two fluids flow. This method assumes that a single cell contains water and air, with a volume fraction a_W and a_A respectively given as Eq. (3.3.1) and Eq. (3.3.2):

$$a_W = \frac{V_W}{V}, \tag{3.3.1}$$

$$a_A = \frac{V_A}{V}, \tag{3.3.2}$$

where V_W and V_A are the volumes of the water and the air, respectively, and V is the total volume of the cell. The summation of a_W and a_A is unity. If $a_W = 0$, the cell unit does not contain water; if $a_W = 1$, the cell unit is filled with water. A cell includes a free surface when $a_W = 0.5$. A weight averaging method is adopted to calculate the density, dynamic viscosity, and velocity of a cell containing water and air, and is given by Eq. (3.3.3) – (3.3.5):

$$\rho = \rho_W a_W + \rho_A a_A, \tag{3.3.3}$$

$$\mu = \mu_W a_W + \mu_A a_A, \tag{3.3.4}$$

$$u_j = \frac{1}{\rho}(u_{W,j}\rho_W a_W + u_{A,j}\rho_A a_A), \tag{3.3.5}$$

where ρ_W and μ_W are the density and dynamic viscosity of water, respectively, and ρ_A and μ_A are the density and dynamic viscosity of air, respectively.

The free surface equation for air and water used in STAR-CCM+ is given by Eq. (3.3.6):

$$\frac{\partial a_i}{\partial t} + u_k \frac{\partial a_i}{\partial x_k} + \nabla \cdot \left(a_i \mathbf{v}_{d,i}\right) + \nabla \cdot \left(a_i(1-a)\mathbf{v}_{c,i}\right) = 0, \tag{3.3.6}$$

doi:10.6342/NTU202304124

where i can be W (water) or A (air), $\mathbf{v}_{d,i}$ is the diffusion velocity, and $\mathbf{v}_{c,i}$ is the sharpening velocity of the edge that is defined as follows:

$$\mathbf{v}_{c,i} = C_a|\mathbf{v}|\frac{\nabla a_i}{|\nabla a_i|}, \tag{3.3.7}$$

where C_a is the sharpening factor.

doi:10.6342/NTU202304124

3.4 Computational Domain and Boundary Conditions

Figure 10 illustrates the dimensions of the computational domain, and Table 3 lists of all boundary conditions employed in the simulation. The top, left, front, and bottom boundaries are velocity inlets, where the initial inflow velocity is set to the ship speed (v_s). The backside boundary condition is a pressure outlet, where the pressure (p_s) is equal to the hydrostatic pressure, being a function of z. Due to that the ship is symmetry to the $y = 0$ plane, a symmetry plane boundary is adopted on the right boundary, i.e., $y = 0$, to reduce the computational cost. The hull surface is a wall boundary type that follows a no-slip condition on the surface. The IJKL plane is the initial location of the still-water plane, where air and water initially occupy the regions above and below the plane, respectively.

doi:10.6342/NTU202304124

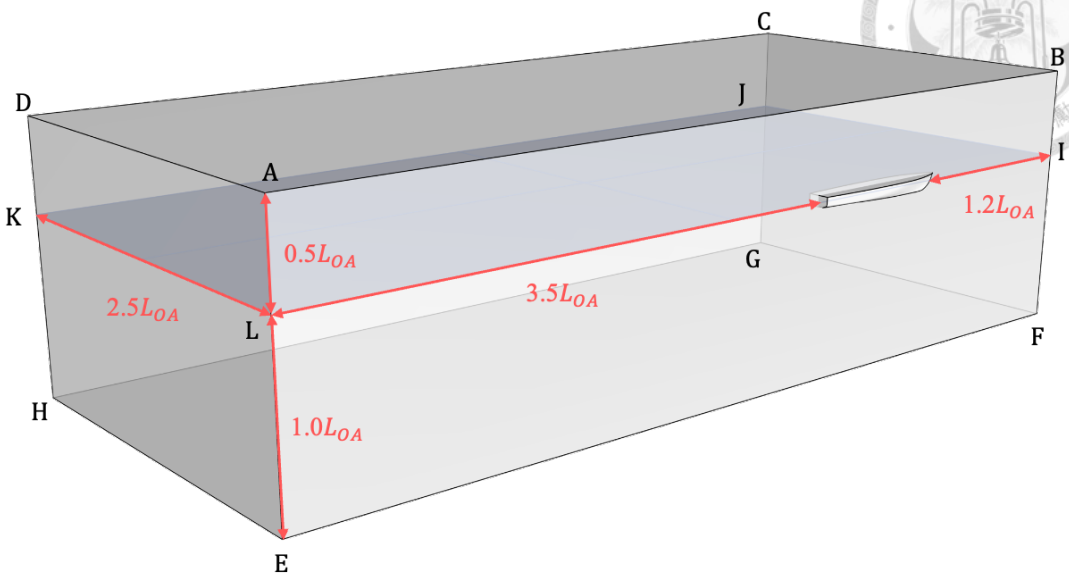

Figure 10: The computational domain

Table 3: Boundary conditions

Surfaces	Boundary types	Boundary conditions
ABCD (top) BCGF (front) EFGH (bottom) DHGC (left)	Velocity inlet	$\mathbf{v} = (-v_s, 0, 0)$
ADHE (back)	Pressure outlet	$p = p_s(z)$
AEFB (right)	Symmetry plane	$\mathbf{v} \cdot \mathbf{n} = 0$
Hull	Wall	$\mathbf{v} = 0$

doi:10.6342/NTU202304124

3.5 Mesh Description

Figure 11 presents the initial mesh cut at $y = 0$ and midship. In this study, a dynamic overset mesh is employed to capture the ship's attitude, where the overset mesh size is approximately 1/20 of the background mesh size. Additionally, a refinement zone is established outside the overset mesh to provide a smooth transition between the overset and background meshes, preventing excessive disparity in mesh sizes that could fail the computations. Figure 12 illustrates the mesh cuts after the simulation. Due to the continuous variation of the free surface location during the simulation, a highly refined grid is necessary to accurately capture its position. However, refining all regions involving the free surface would result in a significant increase in the number of grids, leading to high computational costs. To overcome this, an adaptive mesh refinement (AMR) technique is employed, which automatically detects the location of the free surface and refines the mesh accordingly. With the AMR technique, the simulation can be done using fewer grid points without losing fine flow features.

The AMR module has several distinct characteristics. Firstly, it only refines the volume mesh and does not reconstruct the surface mesh, so it is essential to ensure sufficient density of the surface mesh on the hull surface and hydrofoils. Furthermore, the AMR module not only refines but also keeps and coarsens the mesh when necessary. However, the mesh is not allowed to become coarser than its original density. For grid refinements, the users can impose a limit on the minimum cell size. Thirdly, the AMR module assesses each cell using the criteria based on the flow solution at the current time step to trigger grid manipulation actions. Different criteria are allowed to coexist simultaneously. When a cell satisfies multiple criteria, the grid refinement takes precedence over grid keeping and grid coarsening, while grid keeping takes precedence

doi:10.6342/NTU202304124

over grid coarsening. Finally, each triggering of the AMR module only changes the grid by one grid level at most.

The workflow of the process of AMR is as follows: Firstly, the flow field for the current time step is solved, and evaluation criteria are computed for each cell. Secondly, the evaluation criteria are reduced based on a priority order, and each grid is marked with an indicator indicating “refine,” “coarsen,” or “keep.” Finally, during the occurrence of an AMR event, corresponding adaptations are performed based on the assigned indicators. After the mesh is updated, the flow field solution is interpolated onto the updated mesh.

The evaluation criteria employed in this study consist of two sets: free surface mesh refinement and overset mesh refinement. The evaluation criteria algorithm for the free surface mesh refinement is briefly described below.

First, the gradient of volume fractions used to identify the cells that contain the free surface is calculated for Eq. (3.5.1):

$$|(\nabla a)_W| > \frac{\max(\nabla \alpha_W, \nabla \alpha_A)}{r_i}, \tag{3.5.1}$$

where r_i is a parameter controlling the sensitivity of free surface detection, known as the resolution criterion for interface detection. In this study, r_i is defined as 5. Based on the free surface identification, the cells are initially marked with the indicator I_0. A value of zero ($I_0 = 0$) indicates that the cell does not contain the free surface, while a value of one ($I_0 = 1$) indicates that the cell contains the free surface. The value of I_0 is advected along with the flow field, allowing for the prediction of the upstream or downstream position of the free surface as well as the next time instance of the AMR (T^{UP} and T^{DOWN}) calculation, where T^{UP} and T^{DOWN} can be expressed by Eq. (3.5.2) and (3.5.3):

$$T^{UP} = t + C^{UP} \cdot \Delta t \cdot N_{AMR}, \tag{3.5.2}$$

doi:10.6342/NTU202304124

$$T^{DOWN} = t + C^{DOWN} \cdot \Delta t \cdot N_{AMR}, \tag{3.5.3}$$

where t is the current time instance, Δt represents the time step size, N_{AMR} is the AMR update period, C^{UP} and C^{DOWN} are the swept distance estimation factors for upstream and downstream, respectively. In this study, C^{UP} is set to 0, indicating no upstream prediction is involved, and C^{DOWN} is set to 5. After the trigger time is determined, the value of the final indicator I_{final} for upstream and downstream are computed using two transport equations, as shown in Eq. (3.5.4) and (3.5.5):

$$\frac{\partial I_{final}^{UP}}{\partial t} + u_i^{UP} \frac{\partial I_{final}^{UP}}{\partial x_i} = 0 \tag{3.5.4}$$

$$\frac{\partial I_{final}^{DOWN}}{\partial t} + u_i^{DOWN} \frac{\partial I_{final}^{DOWN}}{\partial x_i} = 0 \tag{3.5.5}$$

The marked region is extended by a certain range (defined by the transition width) to ensure that no invalid mesh arrangements are present. Finally, the update of mesh depends on the comparison between I_{final} and I_0: if I_{final} = I_0 = 1, the original cell size is kept; if I_{final} = 1 and I_0 = 0, the grid is refined; and in other cases, the grid is coarsened.

Figure 13 illustrates the free surface refinement layer and the extended refinement layer, and provides an explanation for the transition width. In this study, the transition width is set to 5.

doi:10.6342/NTU202304124

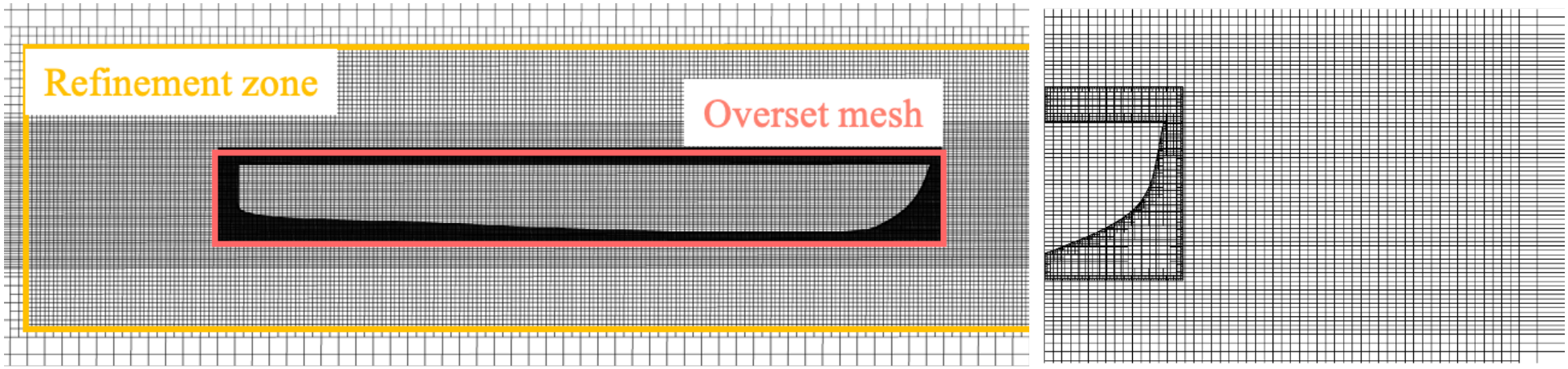

(a) (b)

Figure 11: Initial mesh cut: (a) $y = 0$, (b) Midship

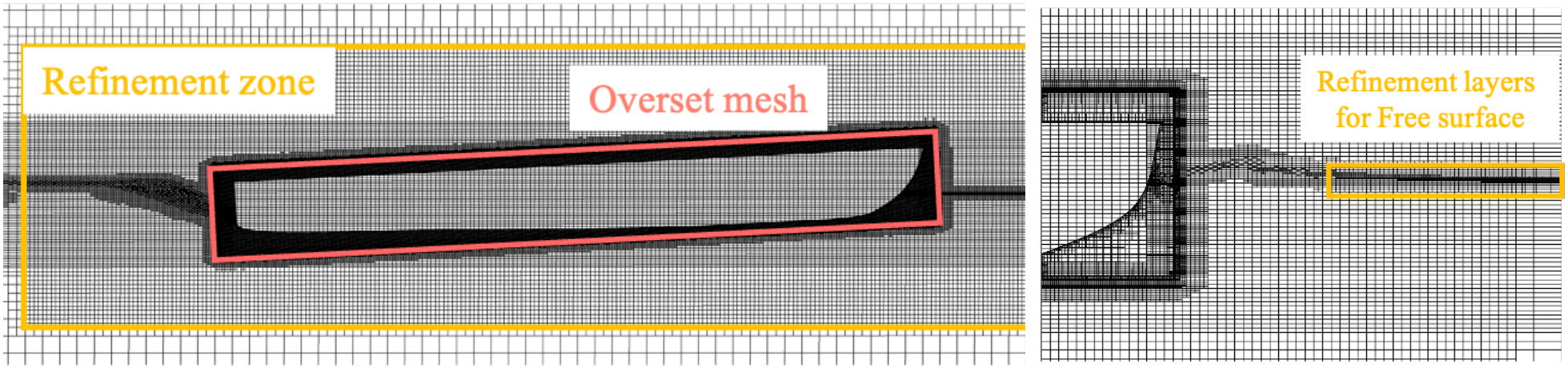

(a) (b)

Figure 12: Final mesh cut: (a) $y = 0$, (b) Midship

doi:10.6342/NTU202304124

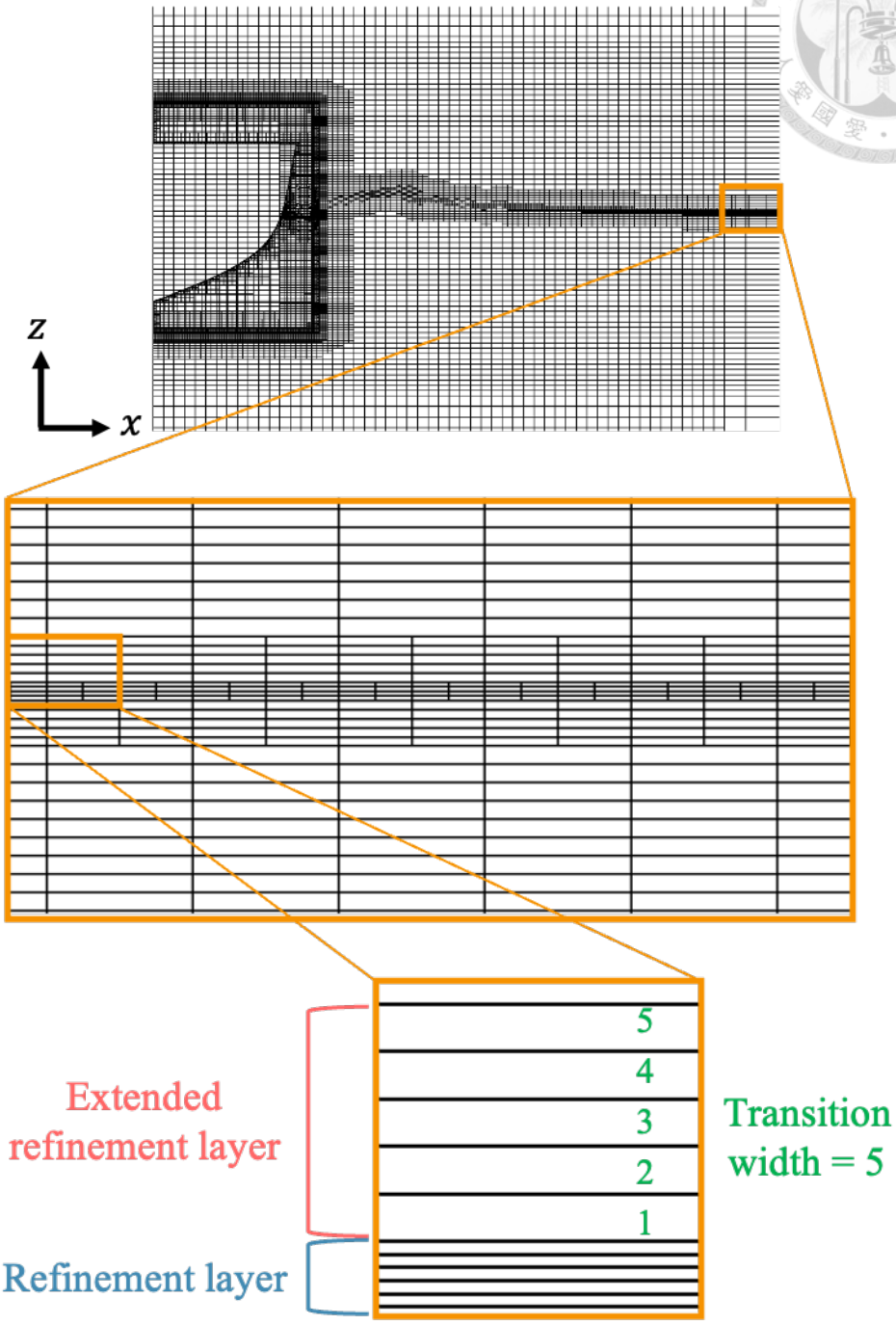

Figure 13: Illustration of adaptive mesh refinement

doi:10.6342/NTU202304124

3.6 Grid Dependency Study

In this study, the discretization error of the grid is analyzed through a grid-dependency study. As there is no analytical solution available for the numerical simulations in this study, Richardson's extrapolation method is employed to predict the grid-independent solution (ϕ^{∞}) as follows:

$$\phi^{\infty} = \phi^{n} + \frac{\phi^{n} - \phi^{n-1}}{\left(\sqrt[3]{\frac{N_n}{N_{n-1}}}\right)^{2} - 1}, \tag{3.6.1}$$

where ϕ^{n} is a generic field variable of the nth grid level, ϕ^{∞} is the grid-independent solution of ϕ and N_n is the total grid number of the nth grid level. This study uses the calm-water ship resistance (R_T) for ϕ. Therefore, Eq. (3.6.1) can be rewritten as Eq. (3.6.2):

$$R_T^{\infty} = R_T^{n} + \frac{R_T^{n} - R_T^{n-1}}{\left(\sqrt[3]{\frac{N_n}{N_{n-1}}}\right)^{2} - 1}, \tag{3.6.2}$$

where R_T^{∞} is the grid-independent ship resistance. Figure 14 presents the ship resistance for each grid level, where the red line indicates R_T^{∞}. Once the grid-independent resistance is obtained, the discretization error ($E_{R_T}^{n}$) and the characteristic cell size for the nth grid level (dx_n) can be analyzed, as shown in Eq. (3.6.3) and (3.6.4):

$$E_{R_T}^{n} = \left|\frac{R_T^{\infty} - R_T^{n}}{R_T^{\infty}}\right|, \tag{3.6.3}$$

$$dx_n = \sqrt[3]{\frac{1}{N_n}}. \tag{3.6.4}$$

Figure 15 shows the relationship between E_{R_T} and dx, where the red line represents the ideal slope of a second-order method. As the grid becomes sufficiently fine, decreasing the cell size causes the error to converge to the ideal slope.

doi:10.6342/NTU202304124

This study requires the establishment of a database comprising thousands of simulated cases, each including the prediction of free-surface behavior. Such an undertaking work demands a significant computational cost. However, due to the AMR technique mentioned in the previous section, it is possible to accurately capture the free-surface behavior using relatively coarse grids. Additionally, it has been confirmed that the surface mesh of the hull form is sufficiently fine to well represent the geometry features, as illustrated in Figure 16. Consequently, the coarsest grid level, where its discretization error is 28.8%, is used in the resistance prediction to achieve higher computational efficiency.

doi:10.6342/NTU202304124

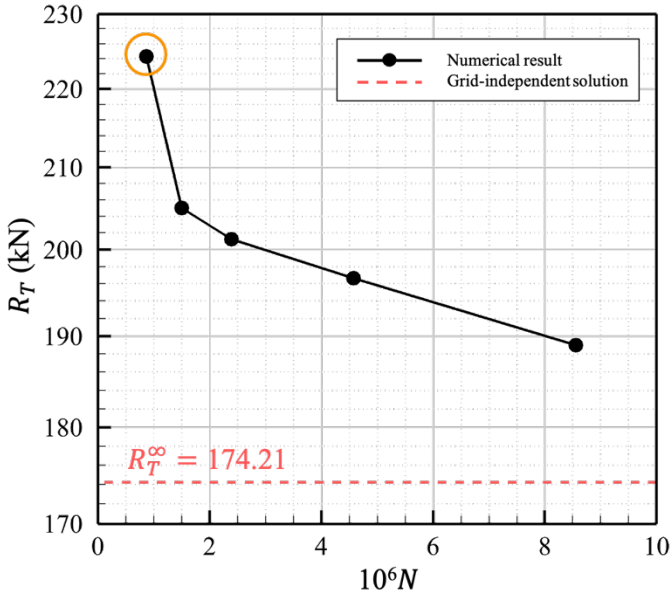

Figure 14: Total resistance of each grid level

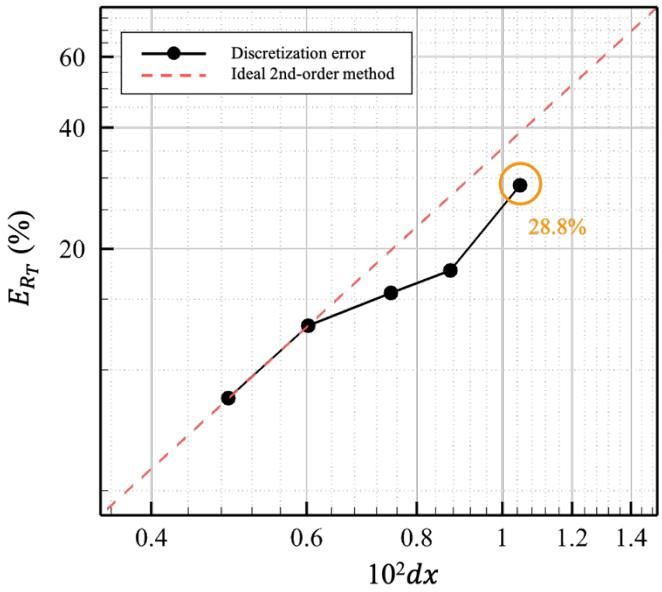

Figure 15: Discretization error with the cell size of each grid level

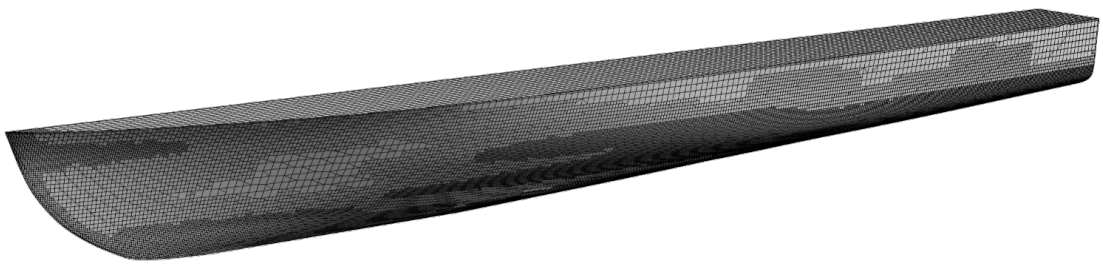

Figure 16: Surface mesh on the NPL hull form

doi:10.6342/NTU202304124

3.7 Experimental Result of NPL Hull Form

This study compares the full-scale ship resistance predicted by CFD and that estimated from the model test to justify the CFD model. As mentioned in previous sections, the model used in this study is the parent hull form 100A from the NPL series, with a scale ratio of 16.21. Detailed ship data of 100A is presented in Table 4, where the subscript "M" denotes the model scale. In the experiment, the longitudinal towing point corresponded to the longitudinal center of buoyancy (LCB) of the ship. The vertical position, on the other hand, referred to the static waterline position. In the NPL design data literature, different hull forms are categorized based on their length-to-beam ratio ($L_{WL,M}/B_{WL,M}$), and resistance curves are plotted for various values of length-displacement ratio (Ⓜ) and displacement Froude number (Fn_{∇}). The corresponding beam-to-draught ratio ($B_{WL,M}/d_M$) is marked beside the respective Ⓜ values. For 100A, $L_{WL,M}/B_{WL,M}$ is 6.25, Ⓜ is 6.585, and under the selected simulation condition, Fn_{∇} is 1.56. Hence, from Figure 17, the model resistance per unit displacement is found to be 0.076, which yields a model resistance of 42.78 N. The way to obtain the running trim angle for the model is similar to the resistance. Thus, from Figure 18, the model's running trim angle (θ) is determined to be 2.08° (by stern).

In this study, the full-scale resistance ($R_{T,S}$) is predicted using a two-dimensional extrapolation procedure [34]. The procedure assumes that the total resistance (R_T) can be decomposed into the residuary resistance (R_R) and the flat-plate resistance (R_F), as Eq. (3.7.3) shows, and the non-dimensional resistance components are defined by Eq. (3.7.4):

$$R_T = R_R + R_F, \tag{3.7.3}$$

$$C_i = \frac{R_i}{0.5\rho_w A_{WET} v_s^2}, \tag{3.7.4}$$

doi:10.6342/NTU202304124

where i is T, R, or F. Assuming that the residuary coefficient is identical at both model and full scale, the total resistance coefficient at full scale can then be predicted. The related coefficients are listed in Eq. (3.7.5) to (3.7.7):

$$C_{T,S} = C_{F,S} + C_{R,S} + \Delta C_F, \tag{3.7.5}$$

$$C_{R,S} = C_{R,M} = C_{T,M} - C_{F,M}, \tag{3.7.6}$$

$$\Delta C_F = 0.044\left[\left(\frac{1.5\times10^{-4}}{L_{WL}}\right)^{\frac{1}{3}} - 10\cdot Re^{-\frac{1}{3}}\right] + 0.000125, \tag{3.7.7}$$

where the subscripts "M" and "S" denote model and full scales, respectively. The roughness allowance, ΔC_F, is given by Eq. (3.7.7). The ITTC 1957 friction coefficient is used for the prediction of C_F.

$$C_F = \frac{0.075}{\log_{10}(Re-2)^2}. \tag{3.7.8}$$

Following the outlined procedures, the full-scale ship resistance of 151.04 kN is estimated from the experiment. Table 5 gives the dimensionless resistance components at the model and full scales.

The numerical ship model and the physical ship model may inevitably exhibit certain geometric discrepancies. Since the running trim angle is sensitive to LCB changes, and the ship resistance is affected by the running trim angle, it is critical to compare the ship resistance of model test and CFD at identical running trim angles. The resistance is predicted based on the model's attitude. By comparing this value with the estimated ship resistance from the model test, an 10.47 % resistance difference is observed, as shown in Table 6. The numerical model tends to overestimate the ship's resistance compared to the model test in this study. However, when comparing the waveforms in Figure 19, both methods show similar pattern in resolving the free surface behavior. Therefore, the numerical model remains reliable despite the overestimation of ship resistance.

doi:10.6342/NTU202304124

Table 4: Model-scale ship data of the NPL hull 100A

$L_{WL,M}$ [m]	d_M [-]	Δ_M [tons]	$L_{WL,M}/B_{WL,M}$ [-]	$B_{WL,M}/d_M$ [-]	Ⓜ [-]	λ [-]	LCB [m]	v_m [m/s]
2.54	0.14	0.057	6.25	2.9	6.585	16.21	1.107	3.026

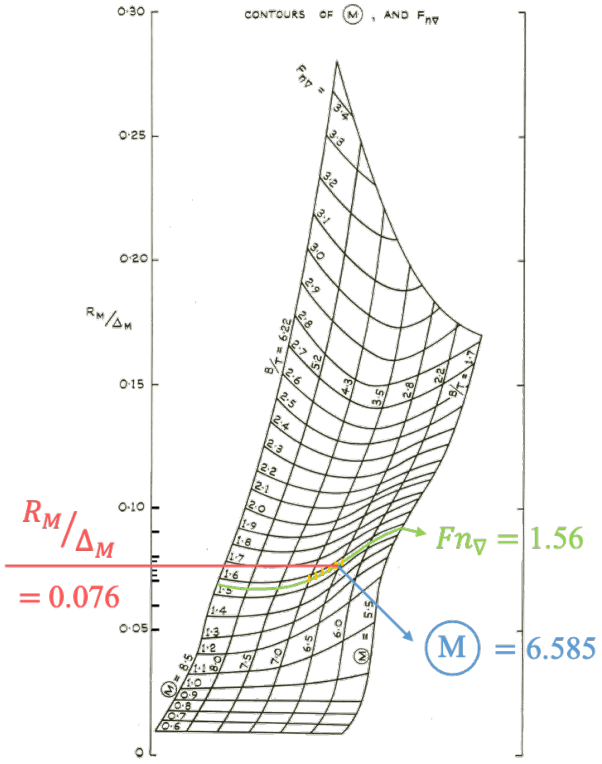

Figure 17: Model resistance of the NPL hull [30]

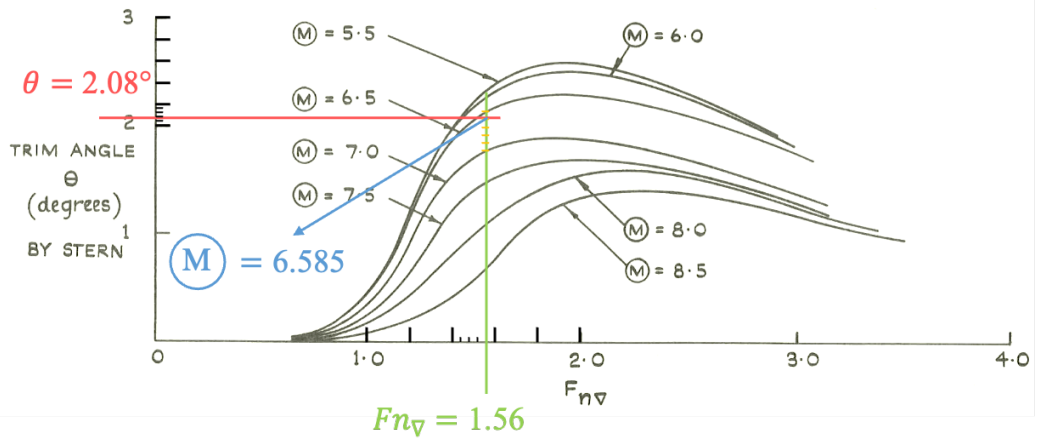

Figure 18: Model running trim angles of the NPL hull [30]

Table 5: Dimensionless resistance components of the NPL hull 100A at $Fn = 0.6$

$10^3C_{T,M}$ [-]	$10^3C_{F,M}$ [-]	$10^3C_{R,M} = 10^3C_{R,S}$ [-]	$10^3C_{F,S}$ [-]	$10^3\Delta C_F$ [-]	$10^3C_{T,S}$ [-]
8.546	3.241	5.305	1.681	0.239	7.225

doi:10.6342/NTU202304124

Table 6: LCB and ship resistance comparison ($Fn = 0.6$)

	LCB (m)	R_T (kN)
Model Test	18.013	151.04
CFD	18.378	167.72
Difference (%)	2.01	10.47

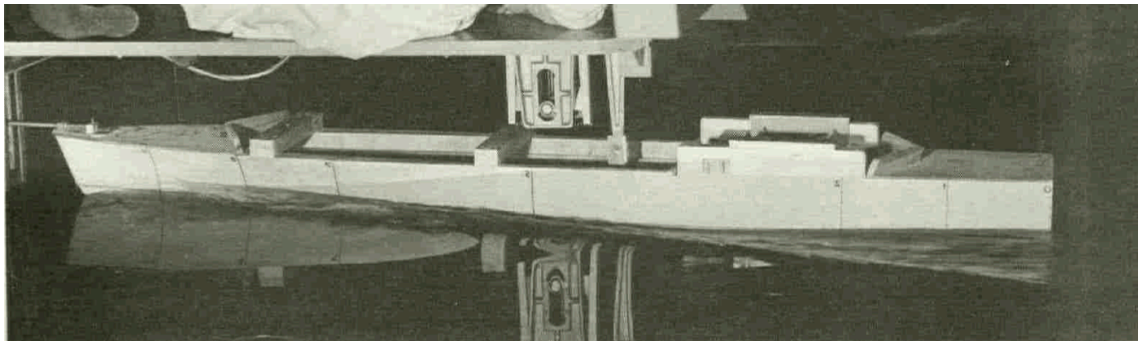

(a)

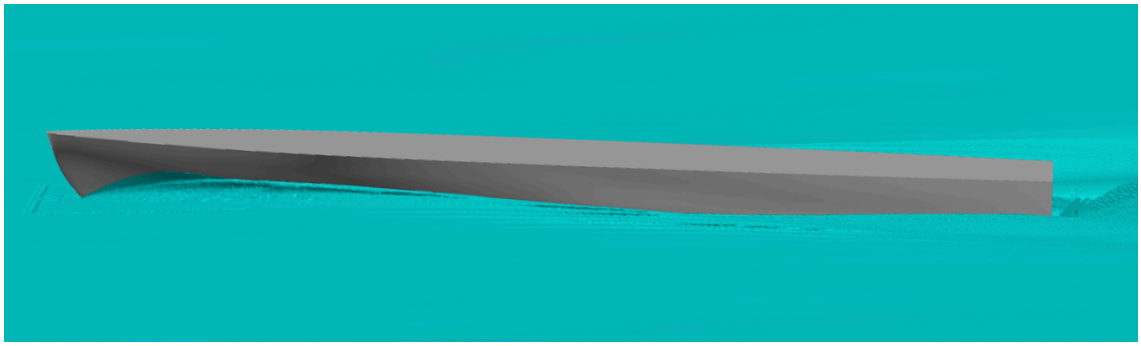

(b)

Figure 19: Wave on the NPL hull: (a) Model test, (b) CFD

doi:10.6342/NTU202304124

3.8 Resistance Prediction

In this section, the CFD results for all investigated cases are summarized. The sign convention for the ship's attitude is presented in Figure 20, where δ is the dynamic sinkage in meters and θ is the running trim angle in degrees.

3.8.1 Hydrofoil Geometry

Figure 21 illustrates the variation of dynamic sinkage and running trim against ship resistance for several aspect ratios with an identical chord length. Correspondingly, Figure 22 displays the cases of different chord lengths with the same aspect ratio. The yellow lines in Figure 21 and Figure 22 denote the ship resistance of the bare hull, and the symbols below the yellow lines indicate successful resistance reduction cases. The lowest resistance in the entire database is 189.06 kN, occurring at $c = 1.51$ and $\Lambda = 1.2$. The dynamic sinkage of the successful resistance reduction cases is found around 0.20 ± 0.05 m, while the running trim of these cases is between -3° and -2°. The cases that are unable to reduce resistance exhibit lower ship resistance at dynamic sinkage close to 0.2 m and running trim between -4° and -3°.

As shown in Figure 21, the ship resistance range increases as the chord length increases. In addition, cases with successful resistance reduction rarely have large chord lengths. Notably, no cases of resistance reduction are observed for $c = 1.81$, and the maximum ship resistance also happens in this group. These results indicate that a chord length greater than 1.81 is apparently beyond the optimized range for the NPL hull form. Figure 22 demonstrates that the ship resistance shows a broader distribution range as the aspect ratio increases. There are still cases of successful resistance reduction at $\Lambda = 1.6$. The number of resistance reduction cases decreases as the aspect ratio or chord length increases.

doi:10.6342/NTU202304124

Figure 21 and Figure 22 show that small or less-slender hydrofoils have better resistance performance because they provide proper lift and generate minor resistance, and large hydrofoils result in more significant resistance.

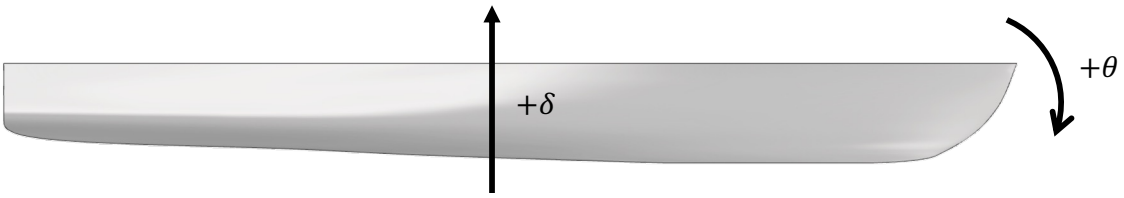

Figure 20: Sign convention of ship attitude

doi:10.6342/NTU202304124

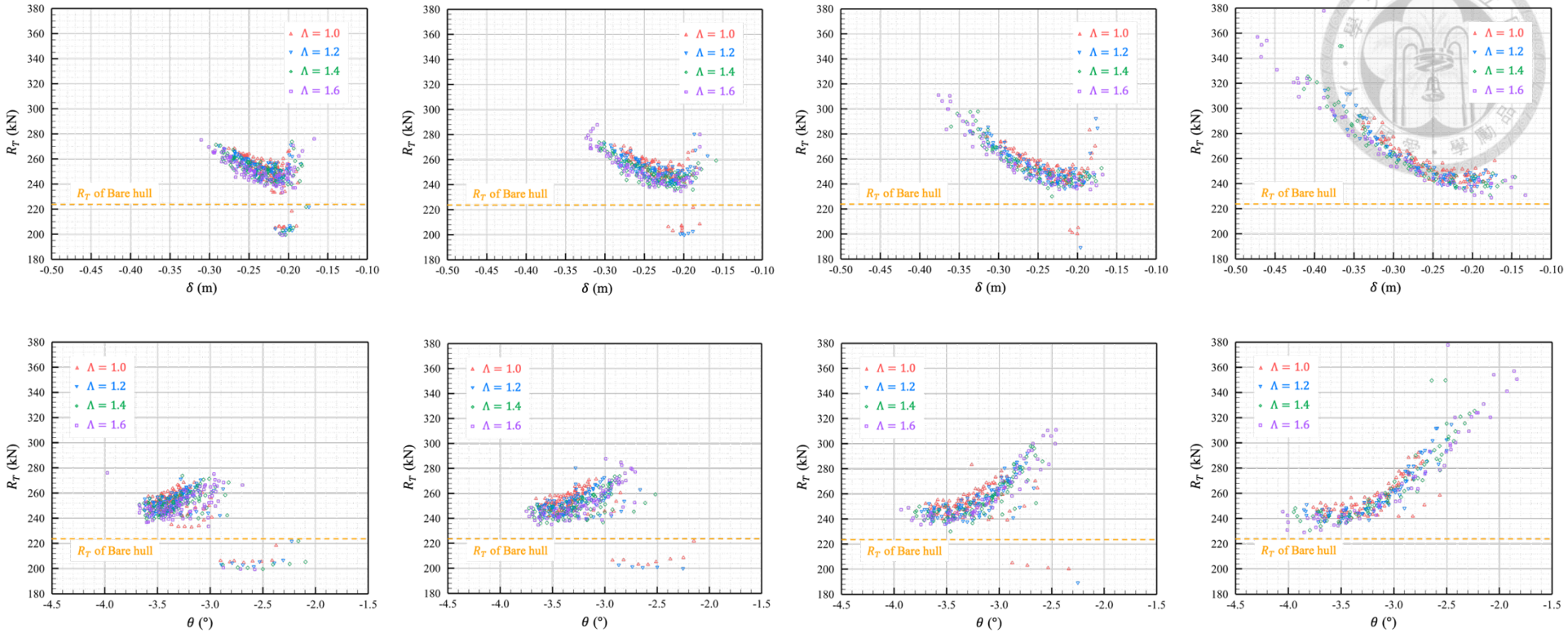

Figure 21: CFD prediction of total resistance: (a) c =1.05 m, (b) c =1.26 m, (c) c =1.51 m, and (d) c =1.81 m

doi:10.6342/NTU202304124

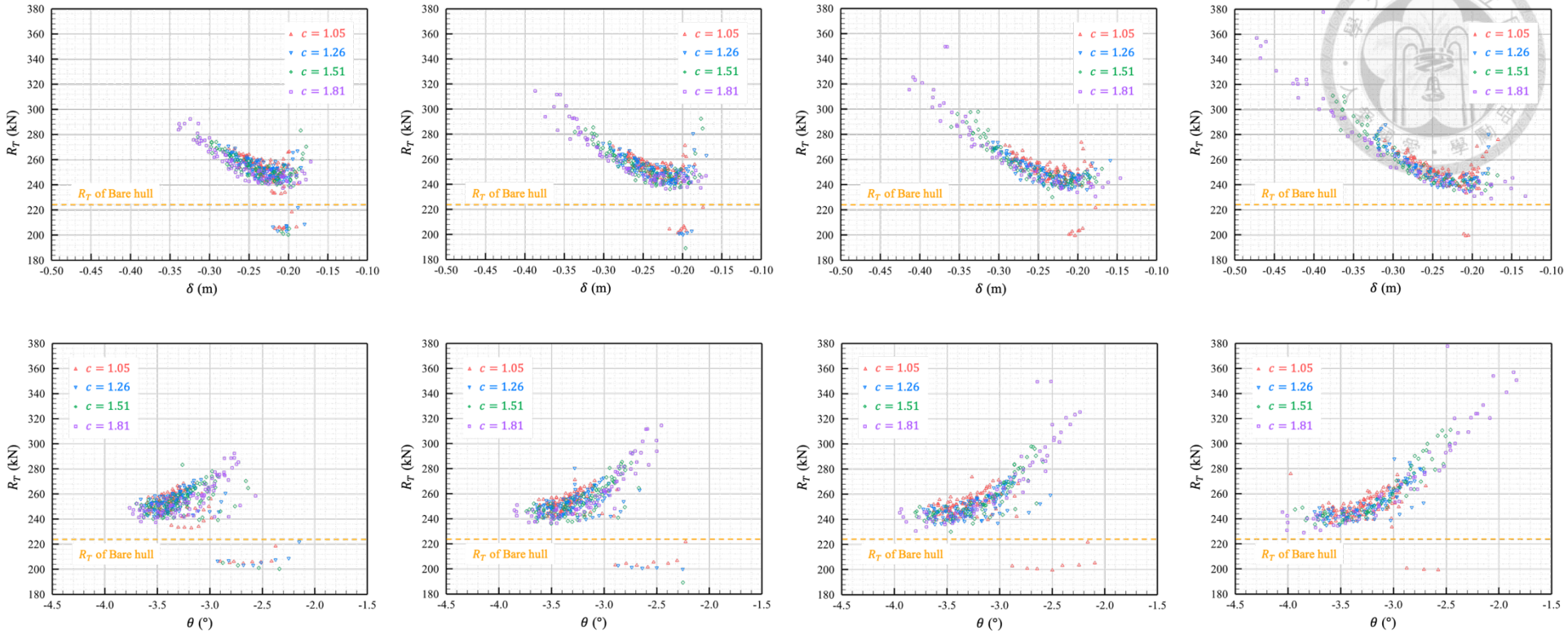

(a) (b) (c) (d)

Figure 22: CFD prediction of total resistance: (a) Λ =1.0, (b) Λ =1.2, (c) Λ =1.4, and (d) Λ =1.6

doi:10.6342/NTU202304124

3.8.2 Hydrofoil Location

Figure 23 and Figure 24 present the scatter plots of the ship resistance against the running trim and dynamic sinkage for different installation locations of hydrofoils. In Figure 23, the cases are grouped based on the vertical position, while in Figure 24, they are grouped based on the longitudinal position. The lowest resistance in the entire data set is 189.06 kN, occurring at $x = 5$ m and $z = 1.0$ m. In Figure 23, the cases with reduced resistance are found near $z = 1.4$ m, indicating that moving the hydrofoil closer to the water surface is more favorable. Figure 24 shows that the resistance grows significantly when the hydrofoil is placed closer to the bow. The cases with reduced resistance are found around $x = 1$, indicating that moving the hydrofoil closer to the stern is more favorable. Although some cases with a bow hydrofoil significantly reduce running trim angles, the accompanied growth in the dynamic sinkage caused excessive drag, leading to the increase of the total resistance.

3.8.3 Summary

Therefore, based on the previous discussions, the following conclusions can be made: a small hydrofoil, a longitudinal location closer to the stern, and a vertical position near the free surface can effectively reduce ship resistance. Small hydrofoils can avoid excessive drag but provide a small lift. Therefore, their placement closer to the stern leads to a long lever arm for generating adequate moment. Further exploration of the underlying factors is presented in the discussion of hydrofoil optimization design.

doi:10.6342/NTU202304124

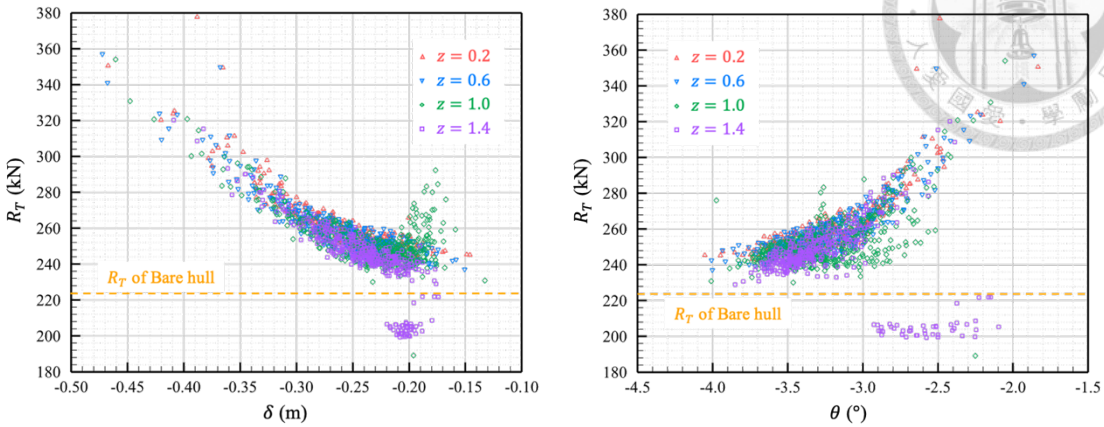

Figure 23: CFD prediction of total resistance at various vertical positions

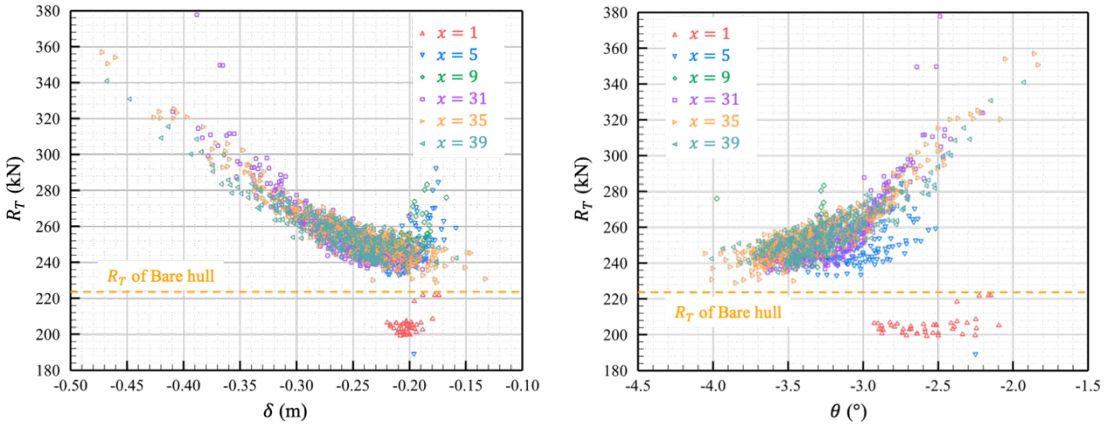

Figure 24: CFD prediction of total resistance at various longitudinal positions

doi:10.6342/NTU202304124

3.9 Computational Cost and Platform

The CFD simulations are performed on a computer cluster. For a database consisting of 1541 cases, the physical computation time is approximately three months. The simulations utilize a coarser grid in conjunction with an adaptive mesh refinement technique, and each case is computed in parallel using two nodes. As a result, the computation time for each case is approximately 8 hours. Detailed specifications of the hardware are listed in Table 7.

Table 7: Hardware Specification

		Cluster
Operating System		CentOS 7.8
CPU	Product	Intel® Xeon® Gold 6326
	No. Cores	32
RAM	Size [GiB]	128
	Clock Rate [MHz]	3200

doi:10.6342/NTU202304124

Chapter 4 DNN Model

4.1 Model Structure

DNN models can be seen as functions that use extensive data to approximate the nonlinear correlation between inputs and outputs, as the form below:

$$\hat{y}_k = DNN(l_i), \tag{4.1.1}$$

where l_i represents the ith input value and $\hat{y}_k$ represents the kth output value. The neurons inside the DNN model adjust different weights and biases to form a well-fitted function. From the aspect of the model structure, an input layer, several hidden layers, and an output layer construct the DNN model, as Figure 25 shows. The hidden layer consists of several neurons, each with different weights corresponding to different input values, and has its own bias. Input values passed into hidden layers are multiplied by a different weight, summed up, added up a bias, and then passed into the transfer function to be the input for the next layer, i.e., m_j^h in Eq. (4.1.2). This process is called forward propagation. If there is only one hidden layer, then the forward propagation can be represented as Eq. (4.1.2) and Eq. (4.1.3):

$$m_j^h = T_g\left(w_{ij}^h l_i + b_j^h\right), \tag{4.1.2}$$

$$\hat{y}_k = P_n\left(w_{jk}^o m_j^h + b_k^o\right), \tag{4.1.3}$$

$$T_g(l) = \frac{2}{1 - e^{-2l}} - 1, \tag{4.1.4}$$

$$P_n(l) = l, \tag{4.1.5}$$

where w_{ij}^h is the weight of a hidden layer (h) as its superscript implies, b_j^h is the bias of a hidden layer, w_{jk}^o is the weight of an output layer (o), and b_k^o is the bias of an output layer. The subscripts i represent the ith input, j means the jth neuron, and k is the kth output. $T_g(l)$ and $P_n(l)$ are two transfer functions, namely the Tansig function and the Purelin

doi:10.6342/NTU202304124

function, respectively; $T_g(l)$ is employed for the hidden layer, and $P_n(l)$ is employed for the output layer. The transfer function aims to add nonlinear properties into the model because the sum-up and add-up processes only deliver linear models.

For data training, the loss function, $e(l)$, is adopted to correct the weight and bias and is defined as follows:

$$e(l) = \sum_{k=1}^{r} (y_k(l) - \hat{y}_k(l))^2, \tag{4.1.6}$$

where $\hat{y}_k$ is the predicted value, y_k is the value from the database, and r is the number of outputs. Once $e(l)$ is obtained, the old weights and biases can be updated to the new values using Eq. (4.1.7) and (4.1.8):

$$\mathbf{w}^{new} = \mathbf{w}^{old} + \mathbf{e}\mathbf{l}^T, \tag{4.1.7}$$

$$\mathbf{b}^{new} = \mathbf{b}^{old} + \mathbf{e}, \tag{4.1.8}$$

where the bolded $\mathbf{w}$, $\mathbf{b}$, $\mathbf{e}$, and $\mathbf{l}$ represent the vector forms of weight, bias, loss function, and inputs, respectively. The calculation process of the loss function and the back-transfer of the correct weight and bias is called backpropagation. Bayesian regularization back-propagation is used in this study.

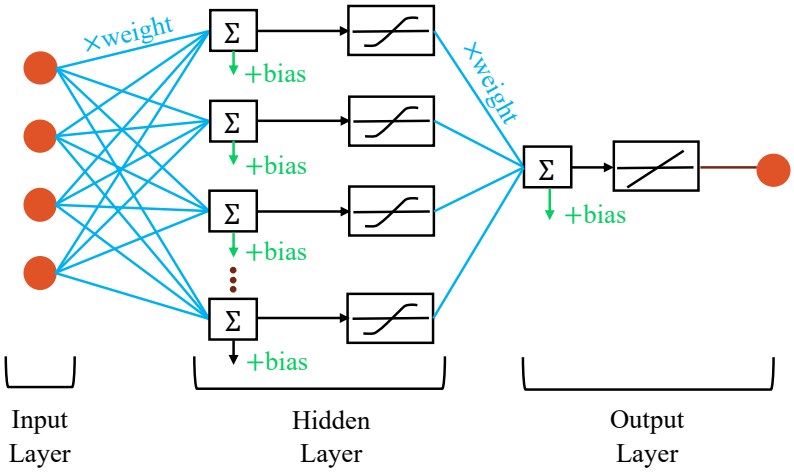

Figure 25: Structure of a DNN model

doi:10.6342/NTU202304124

4.2 Parameters Setting

In this study, a Matlab program is implemented to automatically generate and train DNN models with different numbers of hidden layers and neurons. The workflow of the DNN model construction is depicted in Figure 26.

The maximum number of hidden layers along with the minimum and maximum numbers of neurons per layer are specified to search for proper DNN models. The input layer consists of five design parameters, while the output layer is the corresponding ship resistance. Although the DNN model can accommodate multiple target outputs, this study only uses ship resistance as a single target output due to the need for a larger database when dealing with multiple outputs. For each trained model, its mean absolute percentage error (MAPE) as an indicator to evaluate the model's performance is calculated, as shown in Eq. (4.2.1). Finally, the model with the lowest MAPE from all the trained models is selected as the best-trained model that is used to predict the optimized design parameters of hydrofoils.

$$\text{MAPE} = \left(\frac{1}{r} \sum_{k=1}^{r} \left| \frac{y_k - \hat{y}_k}{y_k} \right| \right) \times 100\%. \tag{4.2.1}$$

In this study, the adopted DNN model is configured with a maximum of five hidden layers. The first two layers are allowed to have 5 to 9 neurons, while the subsequent three layers are allowed to have 3 to 7 neurons. This combination resulted in a total of 3906 DNN models, each with a different number of hidden layers and neurons. If the number of neurons in each layer of the best-trained model is equal to the upper or lower limit of the specified range, the neuron number range is then expanded, and a new search is consequently started. In Figure 27, the total neuron number of all layers of all tested DNN models associated with their MAPE values is presented in a scatter plot. Different colors are used to represent the number of hidden layers used in a DNN model. From Figure 27,

doi:10.6342/NTU202304124

it can be observed that as the number of layers increases, the lowest achievable MAPE also decreases. However, a greater number of layers does not necessarily guarantee a lower MAPE. The best-trained model in this study consists of five hidden layers, each with 8, 7, 6, 5, and 5 neurons, as listed in Table 8. Figure 28 shows a scatter plot of the predicted values from the final model against the corresponding correct values in the database, which is predicted by the CFD computation.

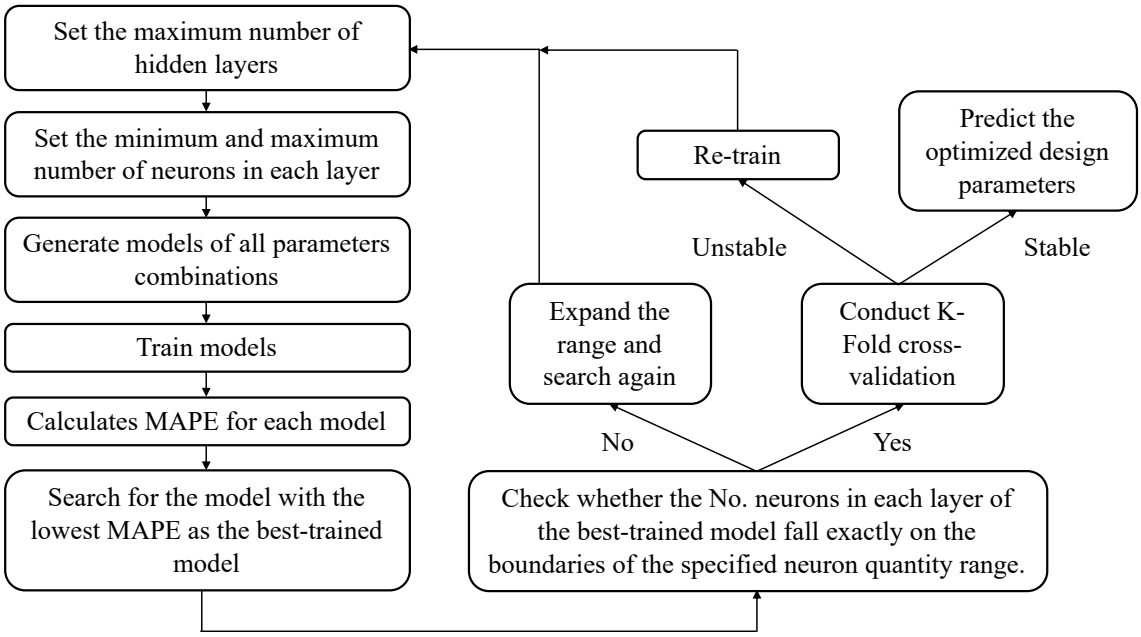

Figure 26: Workflow of DNN model prediction

doi:10.6342/NTU202304124

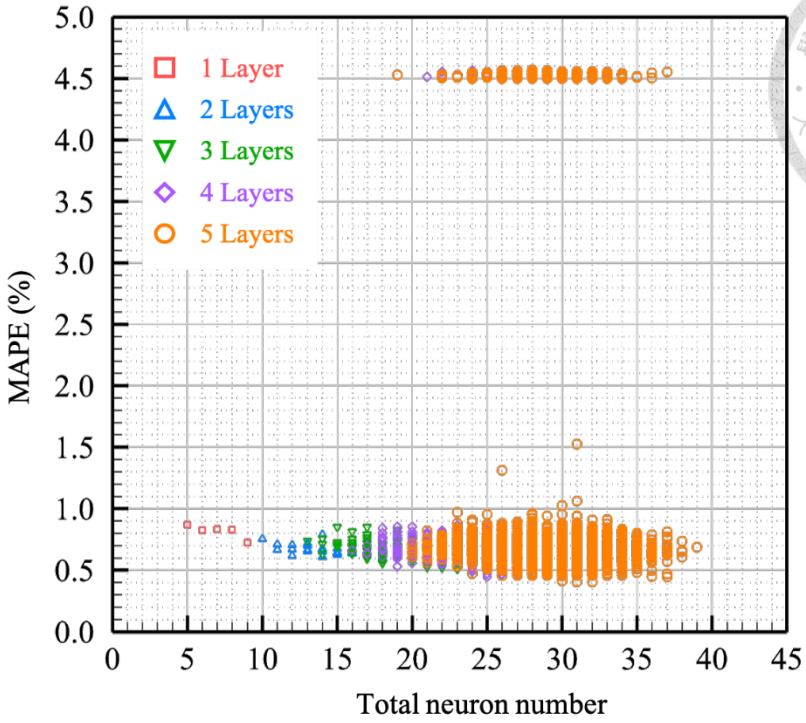

Figure 27: Total neuron number vs. MAPE of various DNN models

Table 8: Neuron number of hidden layers in the proposed DNN model

Hidden layer	1	2	3	4	5
Neuron number	8	7	6	5	5

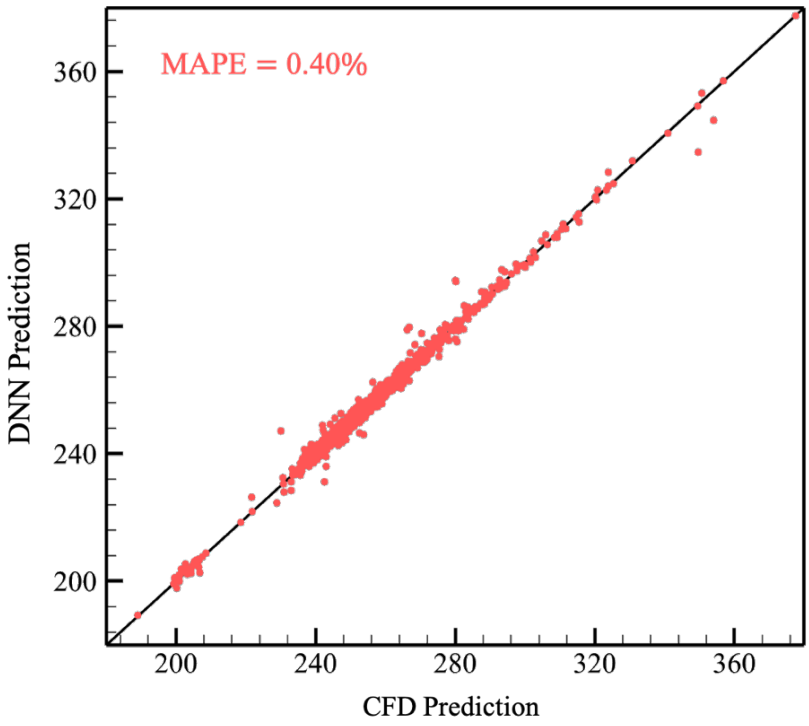

Figure 28: MAPE of the proposed DNN model

doi:10.6342/NTU202304124

4.3 K-fold Cross Validation

To identify the stability of a DNN model, it is necessary to partition the training data into several test data sets to ensure that the training results are independent of the selection of the test data. This study employs a K-fold cross-validation (K-fold CV) for examining the model stability. The schematic plot of a K-fold CV is illustrated in Figure 29. The data is first divided into K parts, and one is used as the test data while the rest $K-1$ parts are used as the training data in each iteration. The MAPE is calculated for each iteration, and the average of MAPE in each iteration is used as the performance indicator of the model. $K = 5$ is chosen in this study, which means 20% of the data is used as the test data in each iteration. The same steps need to be repeated K times (i.e. K iterations), where K data sets are alternately used as testing data.

The result of the K-fold CV is listed in Table 9**,** and plotted in Figure 30. The results of K-fold cross-validation justify the stability of this model, where the MAPE of the training data remains consistent throughout each iteration. Although there is a slight fluctuation in the MAPE of the test data across iterations, their average value is still identical to that of the training data. This suggests that the proposed DNN model successfully avoids the possible overfitting problem.

doi:10.6342/NTU202304124

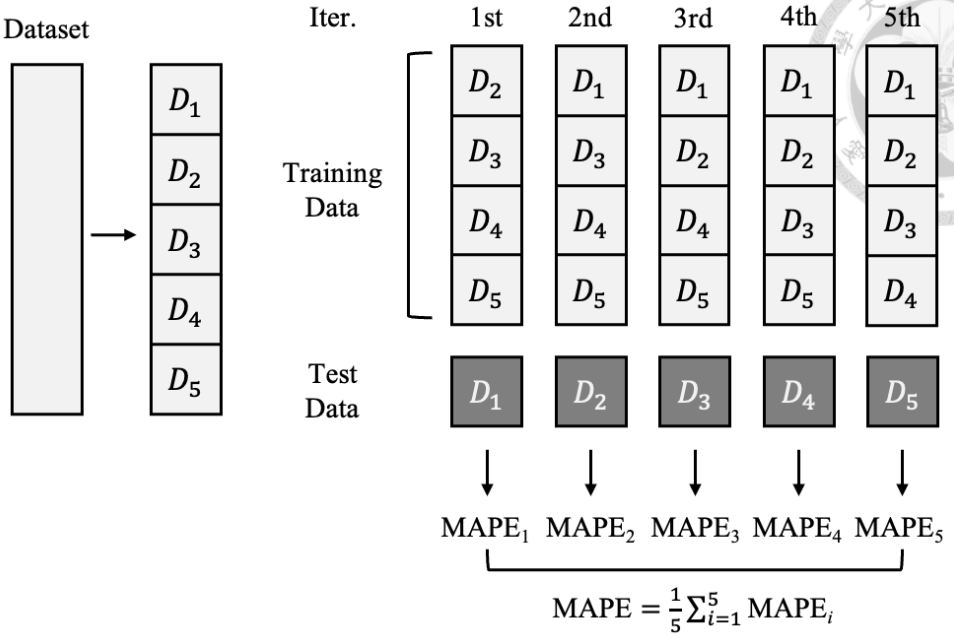

Figure 29: Schematic plot of K-fold CV

Table 9: MAPE in each iteration of K-fold CV

Iteration	1	2	3	4	5	Averaged
Training MAPE (%)	0.39	0.39	0.39	0.39	0.39	0.39
Test MAPE (%)	0.42	0.38	0.40	0.39	0.36	0.39

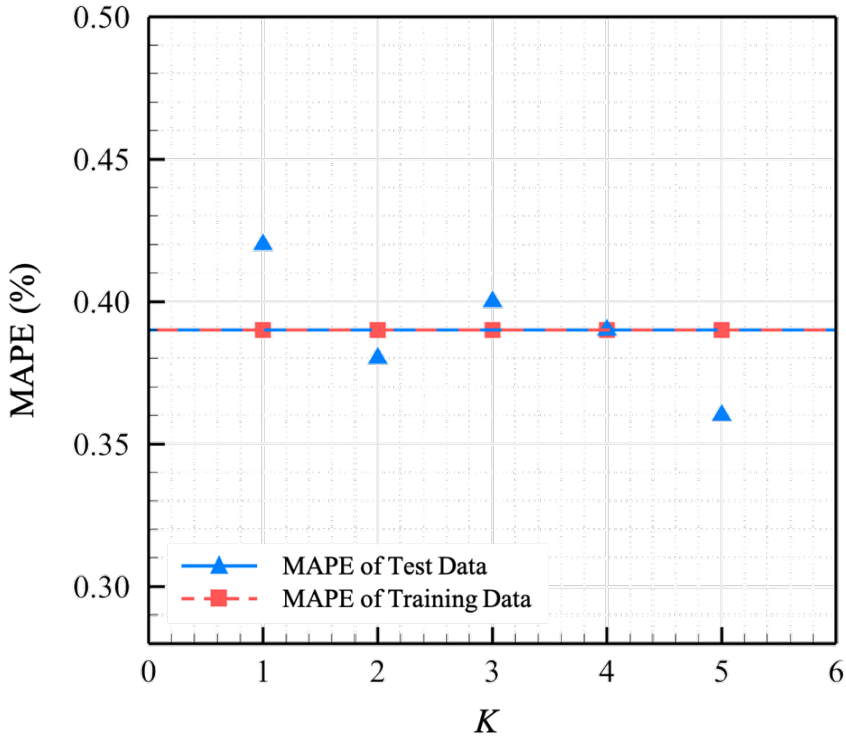

Figure 30: MAPE in each iteration of K-fold CV

doi:10.6342/NTU202304124

4.4 Range of the Optimized Design Parameters

For obtaining optimal design parameters, it is necessary to specify a reasonable search range for each parameter and the target output value. From an optimization perspective, the target value of ship resistance is set to zero, allowing the model to search for the lowest possible resistance and its corresponding design parameters. However, this approach does not deliver reasonable resistance predictions, possibly due to the limited size of the database. Consequently, an alternative strategy is adopted in this study, where the target resistance of 180 kN, representing a 10 kN reduction from the minimum resistance observed in the database, is employed as the first optimization goal. Subsequently, if this target value is achieved, the search continues with an additional 10 kN reduction as the optimization goal. And this approach is iteratively performed until the target resistance becomes zero. Through this approach, the research succeeds in identifying an optimized set of parameters when targeting a resistance of 180 kN.

The prediction range for the parameters is determined by referencing the resistance prediction and the original parameter range from the database. The final prediction range obtained is presented in Table 10. Since there can be a nontrivial difference between the resistance predictions of the DNN and CFD models, 20 sets of optimized design parameters are first selected. These parameter sets are subsequently validated using the CFD model to ensure a resistance reduction is truly achieved.

Table 10: Prediction range of design parameters

x	z	ψ	c	Λ
[m]	[m]	[°]	[m]	[-]
0.5 – 2.8	1.0 – 1.4	0 – 10	1.32 – 1.65	0.8 – 1.4

doi:10.6342/NTU202304124

4.5 Computational Cost and Platform

For training the DNN model, a personal computer is used as the computation platform. The training process utilizes a single core because parallel computing with MATLAB incurs significant data transfer time, which slows down the overall computation process. The training of 3906 DNN models using MATLAB takes approximately 10 hours, while the prediction of the optimized design parameters requires around 20 minutes. Detailed specifications of the hardware are listed in Table 11.

Table 11: Hardware Specification

		Personal Computer
Operating System		Windows 10
CPU	Product	Intel(R) Core(TM) i9-9980XE
	No. Cores	18
RAM	Size [GiB]	128
	Clock Rate [MHz]	3000

doi:10.6342/NTU202304124

doi:10.6342/NTU202304124

Chapter 5 Optimized Design Parameters Predicted by DNN Model

5.1 Resistance Reduction

This section discusses the design parameter sets that the DNN model forecasts to deliver the smallest resistance. The DNN model first predicts 20 different sets of optimized design parameters that may potentially result in resistance reduction. In fact, not all of these parameter sets result in the desired resistance reduction. The reason for the unsatisfactory predictions of the DNN model may come from the complicated interactions between the hull, hydrofoils, and the flow around them because the DNN model training process does not consider flow field information, such as pressure distribution and free surface elevation. Constructing a more extensive database and additionally considering the flow field information to train the DNN model are suggested to improve the DNN model's performance.

Table 12 lists the optimized design parameter set at $Fn = 0.6$, and Table 13 lists the ship resistance predicted by the DNN and CFD models at $Fn = 0.6$. The optimized chord length surpasses the initially anticipated small length, while the aspect ratio aligns with the expected unity. The longitudinal position is close to the stern, and the vertical position is near the water surface as shown in the resistance analysis of a previous section. The resistance predicted by the DNN model differs from that predicted by the CFD model by 3.0%, which is higher than the training error of the DNN model. However, despite the difference, the DNN model successfully predicts the optimized design parameter sets. Table 14 lists the ship resistance and attitude with and without the optimized hydrofoil at $Fn = 0.6$, and Figure 31 illustrates them in a bar chart. The ship resistance predicted by CFD (R_T^{CFD}) can be further decomposed into the pressure resistance (R_P^{CFD}) and the shear

doi:10.6342/NTU202304124

resistance (R_S^{CFD}) as follows:

$$R_T^{CFD} = R_P^{CFD} + R_S^{CFD}. \quad (5.2.1)$$

Under the optimized parameter set, the hydrofoil reduces the running trim angle by 58.4% and the dynamic sinkage by approximately 24.4%, resulting in a 24.9% reduction in the total resistance. Table 14 also shows that the inclusion of the hydrofoil resulted in a 3.2% increase in the shear resistance when compared to the bare hull. Conversely, it led to a substantial 31.5% reduction in pressure resistance as compared to the bare hull, indicating that the hydrofoil successfully leads to a favorable flow field. Furthermore, from the force analysis of the hydrofoil, it generates a lift force of 32.15 kN and a drag force of 26.23 kN at $Fn = 0.6$.

doi:10.6342/NTU202304124

Table 12: Optimized design parameter set at $Fn = 0.6$

c [m]	Λ [-]	ψ [°]	x [m]	z [m]
1.584	1.10	0	0.5	1.2

Table 13: Predicted resistance of the DNN and CFD model at $Fn = 0.6$

R_T^{DNN} [kN]	R_T^{CFD} [kN]	Difference (%)
180.00	174.64	3.00

Table 14: CFD prediction of hull forms w/o the hydrofoils at $Fn = 0.6$

		R_T^{CFD} [kN]	R_P^{CFD} [kN]	R_S^{CFD} [kN]	δ [m]	θ [°]
Bare hull		224.27	186.97	37.30	-0.23	-3.32
With hydrofoil	Hydrofoil	26.23	24.65	1.58	-	-
	Hull	148.41	111.46	36.95	-0.18	-1.82
	Hydrofoil and Hull	174.64	136.11	38.53		
Difference (%)		-24.9	-31.5	3.2	-24.4	58.4

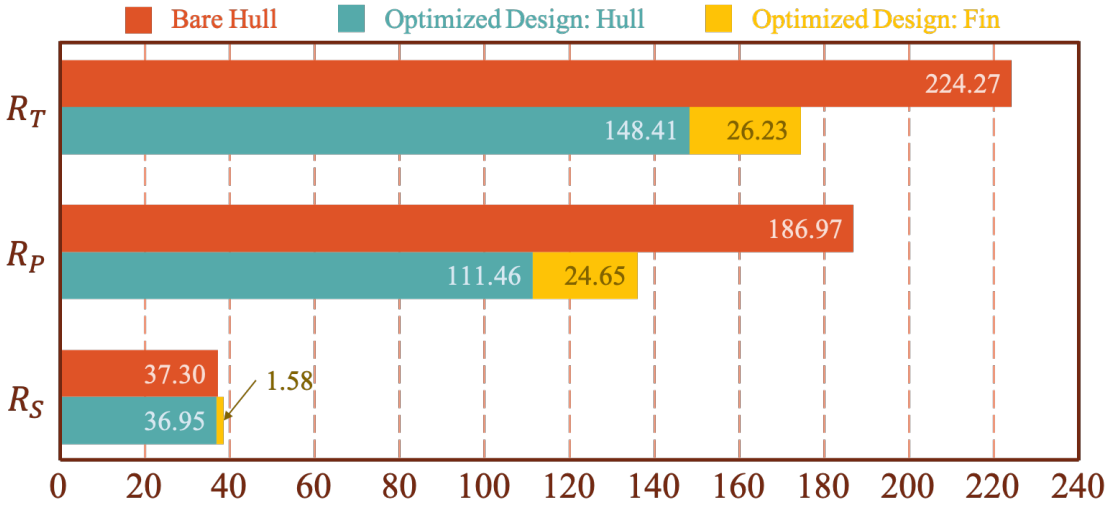

Figure 31: CFD prediction of hull forms w/o the hydrofoils at $Fn = 0.6$

doi:10.6342/NTU202304124

5.2 Flow Field

This study further analyzes the resistance performance by examining the changes in the flow field. Figure 32 and Figure 33 show the dynamic pressure distribution and free surface elevation with and without the optimized hydrofoil at $Fn = 0.6$. The dynamic pressure (p_{dym}) is normalized using the ship speed as the dynamic pressure coefficient, $c_{p,dym}$, according to Eq. (5.2.2). The free surface elevation (η) is normalized using the initial draft according to Eq. (5.2.3).

$$c_{p,dym} = \frac{p_{dym}}{0.5\rho v_s^2}, \tag{5.2.2}$$

$$\eta = {}^{z}/_{d}. \tag{5.2.3}$$

Figure 32 shows that the pressure distribution around the bow of the two ships does not differ significantly, but the ship with hydrofoils has a slightly larger high-pressure zone. The low-pressure zone of the ship with hydrofoils is significantly smaller near the stern, which results in a smaller pressure difference and results in smaller pressure resistance compared to the bare hull. The hydrofoil located near the stern also makes the first wave crest behind the ship further away from the stern.

Since the NPL hull has a high length-to-beam ratio, the ship induced small waves that do not propagate far. Figure 33 shows a wave crest is found at the bow and stern of the ship, and the wave behind the ship has a very small wave height. However, when the optimized hydrofoils are installed, the wave height is even smaller than the case of the bare hull. As shown in Figure 33, the wave trough and the wave crest area near the stern are both significantly smaller than those in the flow field of the bare hull.

doi:10.6342/NTU202304124

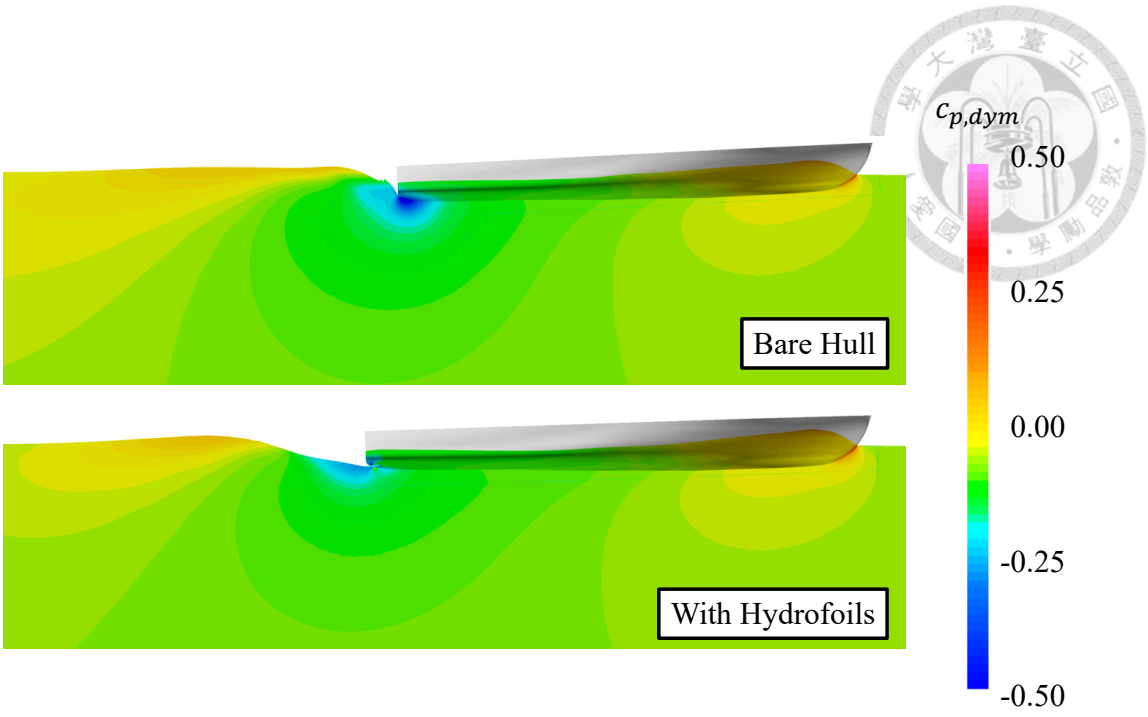

Figure 32: Pressure distribution on hull and flow field at $Fn = 0.6$

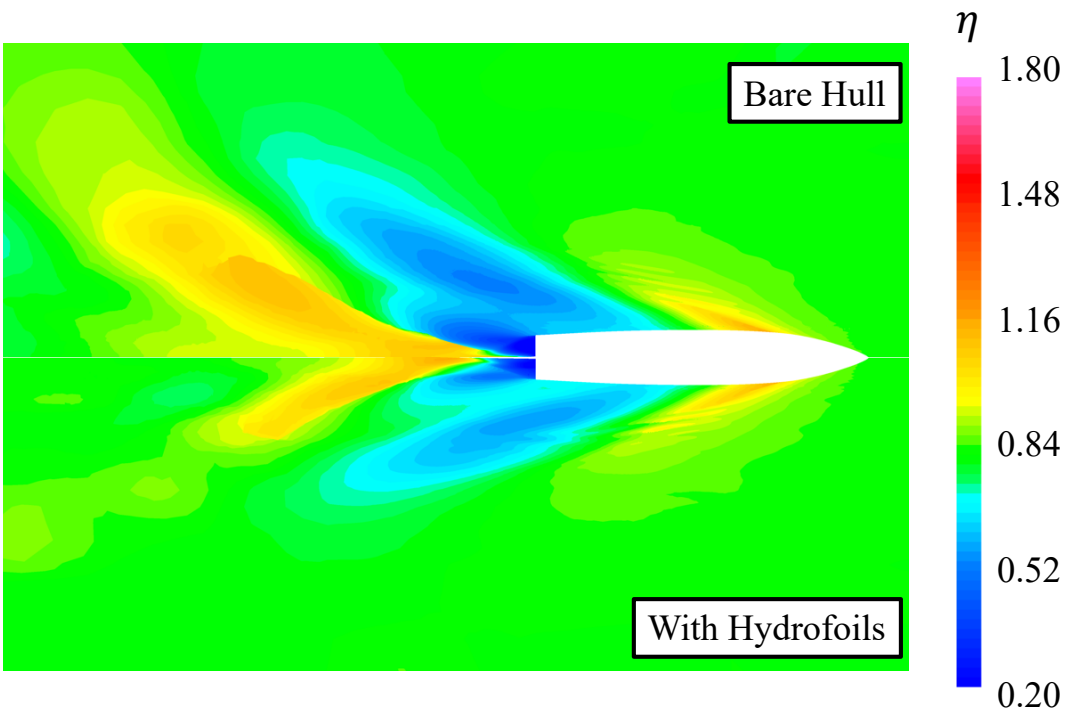

Figure 33: Free surface elevation at $Fn = 0.6$

doi:10.6342/NTU202304124

5.3 Resistance Prediction of Full Speed Range

This study obtains the optimized design parameter set at $Fn = 0.6$. It is interesting to know the impact of the optimized hydrofoils on the total resistance performance at various speeds. This section compares the total resistance of the hull with and without the optimized hydrofoil at $Fn = 0.1$ to 0.9 to investigate the influence of the hydrofoils on the resistance reduction over a wide speed range. Figure 34 and Table 15 show the ship resistance, dynamic sinkage, and running trim with and without the optimized hydrofoil at nine investigated speeds. Two hull forms exhibit significant dynamic sinkage at $Fn = 0.4$ to 0.6, and above $Fn = 0.8$. Without the hydrofoils, the running trim angle grows significantly with increasing speed. Because the hydrofoil attributes reduce the running trim, lower ship resistance is found for speeds above $Fn = 0.4$.

For the NPL hull form, the running trim angle steadily increases with speed in the studied speed range. Therefore, installing hydrofoils is able to reduce the running trim for most speeds. Additionally, the frictional resistance is negligible due to the small size of the selected hydrofoils. Consequently, the optimized design parameter set for hydrofoils can effectively reduce the total resistance for middle and high speeds. However, if other hulls different from the NPL hull are selected, the optimized hydrofoils may likely only reduce the total resistance at the target speed. In conclusion, although the optimization method proposed in this study successfully reduces the total resistance of the NPL hull form at most speeds, further research is needed to find a robust approach to optimize the total resistance considering all speeds.

doi:10.6342/NTU202304124

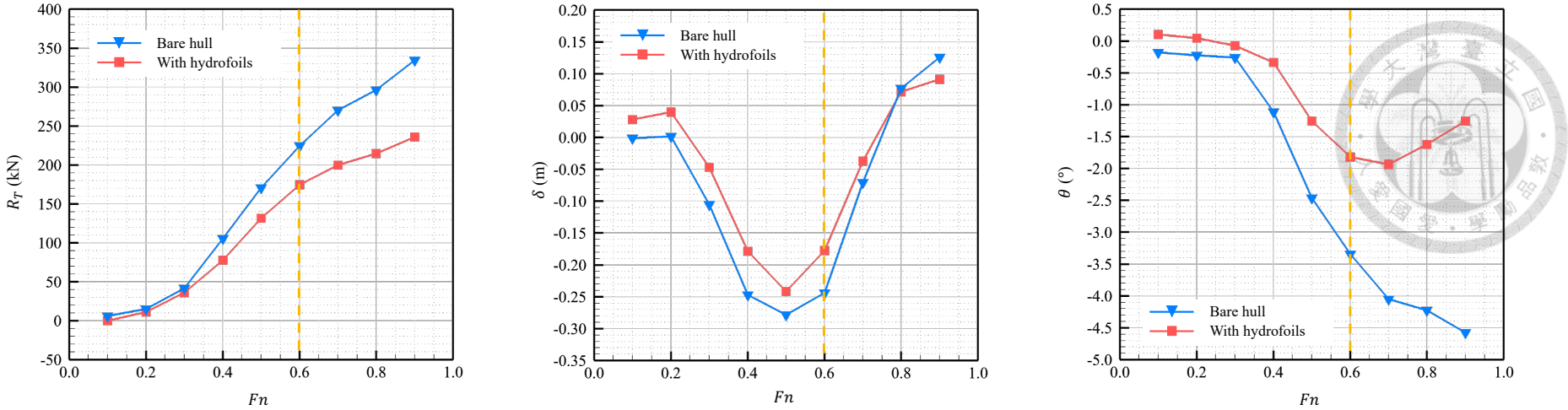

(a) (b) (c)

Figure 34: Comparison between hulls w/o optimized hydrofoil at various Fn: (a) R_T, (b) δ, and (c) θ

Table 15: Comparison between hulls w/o optimized hydrofoil at various Fn: (a) R_T (kN), (b) δ (m), and (c) θ (°)

Fn	With Hydrofoil	Bare Hull	Difference (%)
0.1	0.11	6.12	-193.0%
0.2	11.15	15.37	-31.8%
0.3	36.10	41.56	-14.1%
0.4	77.90	105.59	-30.2%
0.5	131.73	170.61	-25.7%
0.6	174.64	224.27	-24.9%
0.7	199.97	270.06	-29.8%
0.8	214.58	296.47	-32.0%
0.9	236.06	334.38	-34.5%

(a)

Fn	With Hydrofoil	Bare Hull	Difference (%)
0.1	0.028	-0.001	212.2%
0.2	0.040	0.002	182.5%
0.3	-0.047	-0.105	-77.1%
0.4	-0.178	-0.247	-32.2%
0.5	-0.242	-0.278	-14.1%
0.6	-0.178	-0.230	-24.4%
0.7	-0.037	-0.071	-62.2%
0.8	0.071	0.077	-7.6%
0.9	0.091	0.126	-32.2%

(b)

Fn	With Hydrofoil	Bare Hull	Difference (%)
0.1	0.10	-0.18	-729.4%
0.2	0.05	-0.22	-308.5%
0.3	-0.07	-0.26	-113.0%
0.4	-0.34	-1.11	-106.7%
0.5	-1.25	-2.46	-65.1%
0.6	-1.82	-3.32	-58.4%
0.7	-1.93	-4.05	-70.7%
0.8	-1.62	-4.23	-89.1%
0.9	-1.26	-4.57	-113.9%

(c)

doi:10.6342/NTU202304124

doi:10.6342/NTU202304124

Chapter 6 Conclusion

This study aims to investigate the influence of hydrofoils on the resistance performance of a high-speed displacement monohull where a DNN model is used to predict the optimized design parameters for resistance reduction. CFD is used to predict the total resistance under different design parameters, and a database with 1541 cases is established. The database is used to train the DNN model, and the best-trained model consists of five layers with five to eight neurons per layer, where the MAPE is 0.40%. The model successfully predicts design parameters that reduce ship resistance by up to 24.9%. The findings of this study indicate that placing the hydrofoils at the stern of the ship results in a better resistance performance than placing them at the bow. While both positions reduce the running trim angle, placing them at the bow increases the dynamic sinkage, thus increasing total resistance. Furthermore, the resistance component reveals that the additional drag caused by the installation of hydrofoils is not significant within the scope of this study. The primary impact of the hydrofoils on the total resistance is through the lift force that achieves a favorable ship attitude. Although this study focuses on $Fn = 0.6$, installing the hydrofoil can reduce the ship resistance by 14.1% to 34.5% at speeds in the range of $Fn = 0.3$ to 0.9, while it reduces the running trim angle by 58.4% to 113.9 %.

This study has several contributions. Firstly, this study successfully applies the DNN model in predicting optimized design parameters. Although there is a 3.0% difference between the CFD results and the predictions of the DNN model, the DNN model effectively captures the trend between design parameters and ship resistance. This study also successfully proposes an integrated design method for hydrofoils, and investigates the impact of hydrofoils on the resistance performance using the neural networks.

doi:10.6342/NTU202304124

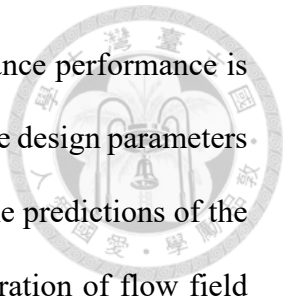

However, this study also has limitations. Firstly, the ship resistance performance is optimized at a fixed speed, not for the entire speed range. Secondly, the design parameters of hydrofoils need to be discussed more comprehensively. Thirdly, the predictions of the DNN model are not sufficiently accurate due to the lack of consideration of flow field information. If the model training process considers the flow field properties, such as pressure distribution, free surface elevation, or nominal wake, it may lead to more accurate predictions. Lastly, although the AMR technique significantly reduces the computational cost of the total resistance database, establishing the total resistance database still requires substantial computation. Future research is suggested to explore methods for simultaneously optimizing the resistance performance under multiple ship speeds. Additionally, GPU acceleration can be employed to expedite the total resistance database construction process. Moreover, the utilization of flow field data for the DNN model training along with sufficiently large databases for multi-objective model training holds the potential to enhance the model's generalization and predictive capabilities.

doi:10.6342/NTU202304124

Reference

[1] M. Sadeghi and H. Zeraatgar, "Investigation on the Effect of Anti-Pitch Fins for Reducing the Motion and Acceleration of Ships Using Computational Fluid Dynamics," *Ocean Engineering,* vol. 267, 2023/01/01 2023, doi: https://doi.org/10.1016/j.oceaneng.2022.112965.

[2] B. R. Reguram, S. Surendran, and S. K. Lee, "Application of Fin System to Reduce Pitch Motion," *International Journal of Naval Architecture and Ocean Engineering,* vol. 8, no. 4, pp. 409-421, 2016.

[3] R. Yao, L. Yu, Q. Fan, and X. Wang, "Experimental and Numerical Resistance Analysis for a Cruise Ship W/O Fin Stabilizers," *Journal of Marine Science and Engineering,* vol. 10, no. 8, 2022. [Online]. Available: https://www.mdpi.com/2077-1312/10/8/1054.

[4] J. H. Lee, I. S. Kim, and D. W. Park, "A Study on the Resistance Performance and Flow Characteristic of Ship with a Fin Attached on Stern Hull," *Journal of the Korean Society of Marine Environment & Safety,* vol. 27, no. 7, pp. 1106-1115, 2021.

[5] P. Sahoo, *Drag Reduction of NPL Round Bilge Hull Forms in HYSUCAT Configuration: An Analytical Study*. 2010.

[6] P. Paialunga. "Deep Learning vs Linear Regression." https://towardsdatascience.com/deep-learning-vs-linear-regression-ea74aca115ea

[7] A. Sherstinsky, "Fundamentals of Recurrent Neural Network (RNN) and Long Short-Term Memory (LSTM) Network," *Physica D: Nonlinear Phenomena,* vol. 404, 2020/03/01 2020, doi: https://doi.org/10.1016/j.physd.2019.132306.

[8] S. Labs. "Understanding Deep Learning: DNN, RNN, LSTM, CNN and R-CNN." https://medium.com/@sprhlabs/understanding-deep-learning-dnn-rnn-lstm-cnn-and-r-cnn-6602ed94dbff

[9] A. I. Georgevici and M. Terblanche, "Neural Networks and Deep Learning: A Brief Introduction," *Intensive Care Medicine,* vol. 45, no. 5, pp. 712-714, 2019/05/01 2019, doi: 10.1007/s00134-019-05537-w.

[10] P. Wang, Z. Chen, and Y. Feng, "Many-Objective Optimization for a Deep-Sea Aquaculture Vessel Based on an Improved RBF Neural Network Surrogate Model," *Journal of Marine Science and Technology,* vol. 26, no. 2, pp. 582-605, 2021/06/01 2021, doi: 10.1007/s00773-020-00756-z.

[11] Y. Wang, J. Joseph, T. P. Aniruddhan Unni, S. Yamakawa, A. Barati Farimani, and K. Shimada, "Three-Dimensional Ship Hull Encoding and Optimization via Deep Neural Networks," *Journal of Mechanical Design,* vol. 144, no. 10, 2022, doi: 10.1115/1.4054494.

[12] D. Yu and L. Wang, "Hull Form Optimization with Principal Component Analysis and Deep Neural Network," *ArXiv Preprint,* 2018.

[13] J. H. Kim *et al.*, "Prediction of the Superiority of the Hydrodynamic Performance of Hull Forms Using Deep Learning," *International Journal of Naval Architecture and Ocean Engineering,* vol. 14, 2022.

[14] M. Mittendorf, U. D. Nielsen, and H. B. Bingham, "The Prediction of Sea State Parameters by Deep Learning Techniques Using Ship Motion Data," in *7th World Maritime Technology Conference 2022*, 2022.

[15] C. P. Tsai, C. Lin, and J. N. Shen, "Neural Network for Wave Forecasting Among

doi:10.6342/NTU202304124

Multi-Stations," *Ocean Engineering,* vol. 29, no. 13, pp. 1683-1695, 2002/10/01 2002, doi: https://doi.org/10.1016/S0029-8018(01)00112-3.
[16] P. Romero-Tello, J. E. Gutiérrez-Romero, and B. Serván-Camas, "Prediction of Seakeeping in the Early Stage of Conventional Monohull Vessels Design Using Artificial Neural Network," *Journal of Ocean Engineering and Science,* 2022/06/18/ 2022, doi: https://doi.org/10.1016/j.joes.2022.06.033.
[17] Y. C. Liu, W. Y. Duan, L. M. Huang, S. L. Duan, and X. W. Ma, "The Input Vector Space Optimization for LSTM Deep Learning Model in Real-Time Prediction of Ship Motions," *Ocean Engineering,* vol. 213, 2020/10/01 2020, doi: https://doi.org/10.1016/j.oceaneng.2020.107681.
[18] M. H. Rashid, J. Zhang, and M. Zhao, "Real-time Ship Motion Forecasting Using Deep Learning," in *The 2nd International Conference on Computing and Data Science*, 2021, pp. 1-5.
[19] E. Rizzuto and V. Ruggiero, "Deep Neural Network (DNN) Method to Predict the Displacement Behavior of Neutral Axis for Ships in Vertical Bending," in *Technology and Science for the Ships of the Future: Proceedings of NAV 2022: 20th International Conference on Ship & Maritime Research*, 2022, vol. 6: IOS Press, p. 95.
[20] H. Cui, O. Turan, and P. Sayer, "Learning-based Ship Design Optimization Approach," *Computer-Aided Design,* vol. 44, no. 3, pp. 186-195, 2012/03/01 2012, doi: https://doi.org/10.1016/j.cad.2011.06.011.
[21] J. Khairuddin, A. Maimun, K. Hiekata, C. L. Siow, and A. Ali, "Web Application with Data Centric Approach to Ship Powering Prediction Using Deep Learning," *Software Impacts,* vol. 11, 2022.
[22] J. B. Lee, M. I. Roh, and K. S. Kim, "Prediction of Ship Power Based on Variation in Deep Feed-Forward Neural Network," *International Journal of Naval Architecture and Ocean Engineering,* vol. 13, pp. 641-649, 2021/01/01 2021, doi: https://doi.org/10.1016/j.ijnaoe.2021.08.001.
[23] L. Lei, Z. C. Wen, and Z. B. Peng, "Prediction of Main Engine Speed and Fuel Consumption of Inland Ships Based on Deep Learning," in *Journal of Physics: Conference Series*, 2021, vol. 2025, no. 1: IOP Publishing.
[24] S. H. Kim, "A Study on the Method for the Estimation of Energy Efficiency Operational Indicator of a Ship Based on Technologies of Big Data and Deep Learning," Seoul National University Graduate School, 2018.
[25] P. van Oossanen, J. Heimann, J. Henrichs, and K. Hochkirch, "Motor Yacht Hull Form Design for the Displacement to Semi-Displacement Speed Range," in *Proc. 10th International Conference on Fast Sea Transportation (FAST 2009)*, 2009.
[26] K. Sariöz and E. Sariöz, "Practical Seakeeping Performance Measures for High Speed Displacement Vessels," *Naval Engineers Journal,* vol. 118, no. 4, pp. 23-36, 2006.
[27] "Yachts by Hull Type: Fast-Displacement Yachts." https://sale.ruyachts.com/yachts/featured/hulltype/fast-displacement-yachts/
[28] S. Pacuraru, F. Pacuraru, and A. Presura, "Numerical Investigation on Fast Displacement Ship Hydrodynamics," *IOP Conference Series: Materials Science and Engineering,* vol. 591, 08/14 2019, doi: 10.1088/1757-899X/591/1/012111.
[29] F. Pacuraru, A. Presura, and S. Pacuraru, "Experimental Towing Tank Tests on High Speed Displacement Ship," in *IOP Conference Series: Materials Science and Engineering*, 2020, vol. 916, no. 1: IOP Publishing.
[30] W. J. Marwood, "Design Data for High-Speed Displacement Hulls of Round-

doi:10.6342/NTU202304124

Bilge Form," *NPL Ship Report,* vol. 99, 1969.
[31] S. W. Chau, "Numerical Investigation of Free-Stream Rudder Characteristics Using a Multi-Block Finite Volume Method," *Institut für Schiffbau, Universität Hamburg, Bericht*, Nr. 580, 1997.
[32] M. Kaushik, "Thin Airfoil Theory," in *Theoretical and Experimental Aerodynamics*, M. Kaushik Ed. Singapore: Springer Singapore, 2019, pp. 127-144.
[33] Siemens, "STAR-CCM+ User Guide Version 2020.1.," 2020.
[34] E. V. Lewis, "Principles of Naval Architecture Second Revision," *Jersey: Sname,* vol. 2, pp. 53-62, 1988.

doi:10.6342/NTU202304124